



# Detection of significant climatic precession variability in early Pleistocene glacial cycles

Parker R. Liataud<sup>a,\*</sup>, David A. Hodell<sup>b</sup>, Peter J. Huybers<sup>a</sup>

<sup>a</sup> Department of Earth and Planetary Sciences, Harvard University, Cambridge, MA 02138, United States

<sup>b</sup> Godwin Laboratory for Palaeoclimate Research, Department of Earth Sciences, University of Cambridge, Cambridge CB2 3EQ, United Kingdom

## ARTICLE INFO

### Article history:

Received 17 July 2019

Received in revised form 8 December 2019

Accepted 4 February 2020

Available online xxxx

Editor: L. Robinson

### Keywords:

Milankovitch

Pleistocene

precession

glacial cycle

spectral analysis

orbital forcing

## ABSTRACT

Despite having a large influence on summer insolation, climatic precession is thought to account for little variance in early Pleistocene proxies of ice volume and deep-water temperature. Various mechanisms have been suggested to account for the dearth of precession variability, including meridional insolation gradients, interhemispheric cancellation of ice-volume changes, and antiphasing between the duration and intensity of summer insolation. We employ a method termed Empirical Nonlinear Orbital Fitting (ENOF) to estimate the amplitudes of obliquity and precession forcing in early Pleistocene proxies and their respective leads or lags relative to the timing of orbital variations. Analysis of a high-resolution North Atlantic benthic  $\delta^{18}\text{O}$  record, comprising data from IODP sites U1308 and U1313, indicates a larger precession contribution than previously recognized, with an average precession-to-obliquity amplitude ratio of 0.51 (0.30–0.76 95% confidence interval) in the rate-of-change of  $\delta^{18}\text{O}$  between 3 and 1 Ma. Averaged when eccentricity exceeds 0.05, this ratio rises to 1.18 (0.84–1.53). Additional support for precession's importance in the early Pleistocene comes from its estimated amplitude covarying with eccentricity, analyses of other benthic  $\delta^{18}\text{O}$  records yielding similar orbital amplitude ratios, and use of an orbitally-independent timescale also showing significant precession. Precession in phase with Northern Hemisphere summer intensity steadily intensifies throughout the Pleistocene, in agreement with its more common identification during the late Pleistocene. A Northern Hemisphere ice sheet and energy balance model run over the early Pleistocene predicts orbital amplitudes consistent with observations when a cooling commensurate with North Atlantic sea surface temperatures is imposed. These results provide strong evidence that glaciation is influenced by climatic precession during the late Pliocene and early Pleistocene, and are consistent with hypotheses that glaciation is controlled by Northern Hemisphere summer insolation.

© 2020 Elsevier B.V. All rights reserved.

## 1. Introduction

Adhémar (1842), Croll (1864), and Murphy (1869) each argued in turn that ice ages are initiated by changes in the duration and intensity of the seasons. Adhémar (1842) suggested that long winters support the growth of ice sheets, while Croll (1864) proposed that cold winters are the most favorable, and Murphy (1869) that cool summers, unable to melt the previous winter's snowfall, are responsible. All three yet agreed that “only one hemisphere, the northern or the southern, has a glacial climate at the same time” (Murphy, 1869), citing the important influence of climatic precession on the duration and intensity of seasons. Climatic precession, whose influence is anti-phased between the hemispheres, arises

from the precession of Earth's rotational axis, at a period of 25.7 ky, which when combined with apsidal precession gives an overall period that ranges between 18 and 24 ky. Its effect on climate is modulated by the orbital eccentricity.

Milankovitch (1941) rejected the view that hemispheres were alternately glaciated, arguing instead that a Northern Hemisphere glacial advance has global consequences by changing the planetary albedo. Using more accurate calculations of variations in obliquity – which produce in-phase changes in insolation across both hemispheres – than had been available to his predecessors, Milankovitch predicted the timing of ice ages from variations in the summer caloric half-year, or the insolation averaged over the half of the year that maximizes the resulting value, on which precession and obliquity have nearly equal influence. A number of studies have confirmed Milankovitch's hypothesis in the late Pleistocene; for example, sea-level highstands demonstrate variability consistent with Milankovitch's hypothesized precession phase (e.g.

\* Corresponding author.

E-mail address: [parker\\_liataud@g.harvard.edu](mailto:parker_liataud@g.harvard.edu) (P.R. Liataud).

Broecker et al., 1968), and other climate proxies feature obliquity and precession amplitudes consistent with Milankovitch's hypothesized forcing (Hays et al., 1976; Imbrie et al., 1992). But whether Milankovitch's theory, or indeed any theory calling upon precession as causing fluctuations in ice volume, also holds for the early Pleistocene and late Pliocene is much less clear, because  $\delta^{18}\text{O}$  measured in benthic foraminifera has been interpreted to vary almost exclusively at the obliquity period of 41 ky during this earlier epoch, with apparently negligible variance at precession periods (Ruddiman et al., 1986).

Several explanations have been proposed for the 41-ky ice ages. Raymo and Nisancioglu (2003) proposed that the meridional insolation gradient, which varies primarily at the obliquity period, could drive heat and moisture fluxes that would control the ice sheet mass balance, but this would require that the ice sheet be equally sensitive to insolation in the sub-tropics and at high latitudes. Loutre et al. (2004) asked whether the mean annual insolation, which features no precession variance, could drive long-term climate variability, and also proposed a role for the meridional insolation gradient in driving poleward moisture transport. Huybers (2006), modifying the caloric half-year model of Milankovitch (1941), argued that the influence of precession-induced changes in insolation intensity are canceled by an opposing change in summer duration. The degree of precession cancellation would depend on several factors, including the average global temperature and the meridional extent and thickness of the ice sheet (Huybers and Tziperman, 2008).

Contrasting with explanations excluding precession from the forcing, Raymo et al. (2006), extending the model of Murphy (1869), argued that local summer intensity does control ablation, but its anti-phased response between the hemispheres results in a cancellation of the precession signal in  $\delta^{18}\text{O}$  records. This would require that the Southern Hemisphere contribution to changes in  $\delta^{18}\text{O}$  nearly balance and be well-mixed with that of the Northern Hemisphere despite the Northern ice sheets lying at comparatively low latitude (Alley, 1991), with an ablation margin exposed to insolation more strongly influenced by precession. The foregoing mechanisms are not mutually exclusive, and Tabor et al. (2015) suggested that a combination of factors including eccentricity modulation of the precession amplitude and obliquity's longer period relative to precession increase the obliquity response relative to precession.

Evidence for the presence of precession in early Pleistocene glacial cycles is not entirely absent. An analysis of globally-distributed benthic  $\delta^{18}\text{O}$  records suggested that the amplitude of climate variability at precession frequencies follows the long-term amplitude modulations of climatic precession throughout the Plio-Pleistocene (Lisiecki and Raymo, 2007), and precession has long been identified in early Pleistocene planktonic  $\delta^{18}\text{O}$  records for use in the construction of age models (Shackleton et al., 1990). A further important finding is that not all early Pleistocene glacial cycles are symmetric (Ashkenazy and Tziperman, 2004; Lisiecki and Raymo, 2007), with rates of deglaciation appearing to exceed those of glaciation in some cycles. This asymmetry suggests a nonlinear response to orbital forcing and is qualitatively consistent with late Pleistocene climate variability, albeit of smaller magnitude (Huybers, 2007). Because precession does not change the net annual insolation, only redistributing it across seasons (Rubincam, 1994), its appearance in climate proxies must result from a nonlinearity in the climate response (Rubincam, 2004) or how it is recorded (Huybers and Wunsch, 2003). Precession might therefore be expected to accompany apparently nonlinear variability during the early Pleistocene, just as it does similar asymmetric variability in the late Pleistocene. These factors motivate our revisiting the substantiality of precession forcing in early Pleistocene glacial cycles.

## 2. Data

We evaluate a composite, high-resolution benthic  $\delta^{18}\text{O}$  record from the North Atlantic ocean spanning 3 Ma to the present, referred to as L2H19 (Fig. 3a). L2H19 comprises data from IODP Site U1313 between 3 Ma and 2.42 Ma and from Site U1308 thereafter. The combined record features an average temporal resolution of 0.3 ky from 1.62 Ma to present, 1.3 ky from 2.42 to 1.62 Ma, and 2.1 ky from 3.0 to 2.42 Ma.

The choice to patch U1313 between 3 Ma and 2.42 Ma was made for purposes of having a complete and undistorted record. Although U1308 extends to beyond 3 Ma, it contains a hiatus between 2.6 and 2.65 Ma that skips Marine Isotope Stages (MIS) G1 and G2, and low sedimentation rates or a short hiatus distorts MIS 97 and 98 (Hodell and Channell, 2016). U1313 provides a more complete record in the late Pliocene (Bolton et al., 2010), and its benthic  $\delta^{18}\text{O}$  values closely align with those of U1308 where they overlap except with minor amplitude mismatches from 2.7 to 2.9 Ma. Both records are drilled at similar water depths, with U1313 at 3426 m and U1308 at 3882 m, and the shipboard spliced composite sections were checked for completeness. U1313 and U1308 are spliced together by taking mean values across an overlap of 10 ky at 2.42 Ma (Fig. A.1).

Five other benthic  $\delta^{18}\text{O}$  records that extend into the early Pleistocene are also evaluated, and their characteristics are listed with those of L2H19 in Table 1. Two records, one from DSDP Site 607 and the second from ODP Sites 980 and 981, are from the North Atlantic. The three other records, from ODP Sites 677, 846, and 849, are from the equatorial Eastern Pacific. For completeness, we additionally evaluate the globally-averaged records of Lisiecki and Raymo (2005) and Huybers (2007).

To better ensure that our results neither diminish nor over-represent orbital variability, two separate chronologies are considered, based on orbitally-tuned and depth-derived records (Lisiecki and Raymo, 2005; Huybers, 2007). Details of depth-age relationships are given in Appendix A.

## 3. Indeterminate precession estimates from spectral analysis

### 3.1. Method

Following the convention of past studies (Hays et al., 1976; Imbrie and Imbrie, 1980), we first attempt to quantify orbital forcing of early Pleistocene glacial cycles using spectral analysis, evaluating the rate-of-change of  $\delta^{18}\text{O}$ , i.e.,  $d\delta^{18}\text{O}/dt$ . Analysis of the rate-of-change, rather than the magnitude, follows from major ice sheets having long response times (Weertman, 1964) and is supported by correlation between  $d\delta^{18}\text{O}/dt$  and summer-integrated energy (Roe, 2006; Huybers, 2006). Analyzing  $d\delta^{18}\text{O}/dt$  also permits for better separating sensitivity to orbital forcing from the influence of the relative periods of orbital variations, with previous studies noting that obliquity's longer period amplifies it relative to precession when integrating a model that relates orbital forcing to the rate-of-change of ice volume (Huybers and Tziperman, 2008; Tabor et al., 2015).

$d\delta^{18}\text{O}/dt$  is constructed by taking the first-difference of  $\delta^{18}\text{O}$  then dividing by the time between samples, after linearly interpolating to an even spacing of 0.5 ky. Although some samples in L2H19 are taken at smaller intervals than this, repeating the analysis using a spacing of 0.25 ky leads to only minor differences in estimates. Power spectral density (PSD) is computed using Thomson's multi-taper method with three tapers (Percival and Walden, 1993). A noise floor is estimated by fitting a power law to the PSD (see Fig. 1 and Appendix B). The variance attributed to obliquity and precession is the sum between the power spectrum and the noise floor in their respective frequency bands, defined to be

**Table 1**

Properties of marine sediment cores. Listed are the standard deviation of  $\delta^{18}\text{O}$  between 2 and 1 Ma, location, estimated age of the oldest sample, and mean sampling interval. Age and sampling interval are given as available for both orbitally-tuned and depth-derived age models. The coordinates of L2H19 are listed as those of IODP Site U1308, although between 3 and 2.42 Ma, data are from Site U1313.

Age model Record	$\sigma$ (‰, 2-1 Ma)	Lat. (°)	Lon. (°)	Orbitally-tuned, 3-1 Ma		Depth-Derived, 2-1 Ma		Original reference(s)
				Age (Ma)	$\Delta t$ (ky)	Age (Ma)	$\Delta t$ (ky)	
L2H19	0.37	50N	24W	3.00	0.97	2.0	0.48	Hodell et al. (2008); Bolton et al. (2010); Hodell and Channell (2016)
LR04	0.28	-	-	3.00	2.35	-	-	Lisiecki and Raymo (2005)
H07	0.25	-	-	-	-	2.00	1.00	Huybers (2007)
DSDP 607	0.35	41N	33W	3.00	3.89	2.00	3.55	Ruddiman et al. (1989)
ODP 677	0.31	1N	84W	2.60	1.74	1.95	1.63	Shackleton et al. (1990)
ODP 846	0.29	3S	91W	3.00	2.36	1.77	2.71	Mix et al. (1995a)
ODP 849	0.29	0	111W	3.00	3.20	2.00	3.49	Mix et al. (1995b)
ODP 980/981	0.34	55N	17W	3.00	2.08	1.95	2.85	Oppo et al. (1998); McManus et al. (1999); Mc Intyre et al. (1999); Flower et al. (2000); Raymo et al. (2004)

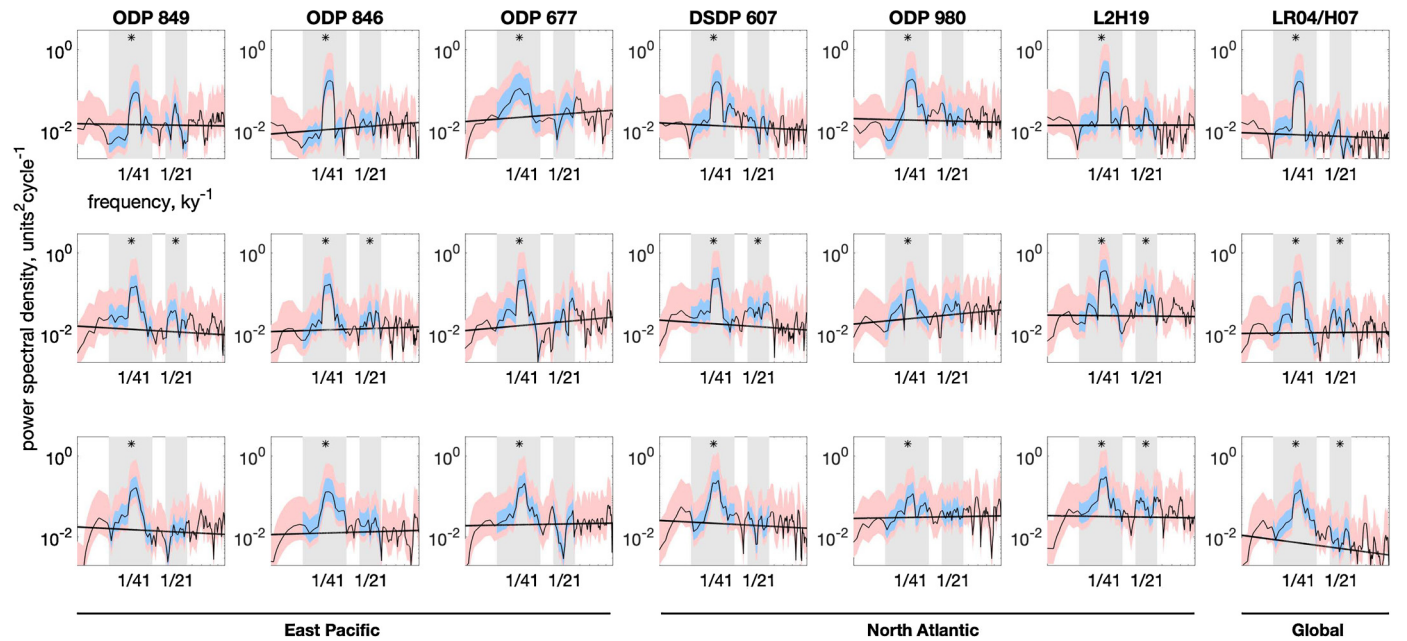


**Fig. 1.** Power spectra of  $d\delta^{18}\text{O}/dt$ . Columns are organized by the longitude associated with each record from west to east, except for L2H19 and LR04/H07 which comprise multiple records. Rows are organized according to spectra for orbitally-tuned timescales for 3-2 Ma (top), orbitally-tuned timescales for 2-1 Ma (middle), and depth-derived timescales for 2-1 Ma (bottom). 95% confidence intervals are shown both for individual spectral estimates (red) and for energy summed across orbital bands (blue; see Appendix B). Bands over which obliquity and precession power are summed (gray shading) are at  $1/41 \pm 1/125 \text{ ky}^{-1}$  and  $1/21 \pm 1/125 \text{ ky}^{-1}$ . All twenty-one obliquity-band spectral power estimates are significant at the 95% confidence level (indicated by black stars), but only seven indicate correspondingly significant climatic precession. In the last column, the upper two panels refer to the LR04 stack, and the bottom panel refers to the H07 stack. (For interpretation of the colors in the figure(s), the reader is referred to the web version of this article.)

$1/41 \pm 1/125 \text{ ky}^{-1}$  and  $1/21 \pm 1/125 \text{ ky}^{-1}$ , including negative values where the noise floor exceeds the power spectrum. Sums are taken as a fraction of the total area under the power spectrum, then multiplied by the time series' variance. The square root of this result is reported in amplitude units of  $0.001\text{‰} \text{ ky}^{-1}$ , or  $\text{meg}^{-1} \text{ ky}^{-1}$ .

Nearly all Pleistocene records feature a red background continuum, with  $\delta^{18}\text{O}$  typically following a spectral power law ranging from 0.8 to 2 that breaks down at or above  $1/100 \text{ ky}^{-1}$  (Wunsch, 2003). A process following a power law of 2 may be produced by a random walk in which its value at the next time-step is the sum of its current value and a random number drawn from a Gaussian distribution. Differencing such a record therefore whitens its spectrum (Bracewell, 1986), consistent with the approximately flat noise floor in  $d\delta^{18}\text{O}/dt$  (Fig. 1).

The 95% confidence interval for the power spectrum is estimated from the approximate  $\chi^2$ -distribution of the spectral es-

timator (Percival and Walden, 1993), with further details given in Appendix B. To obtain approximate upper 95% confidence bounds for orbital amplitudes, the procedure for calculating orbital amplitudes is applied to the upper confidence bound of the power spectrum, and vice-versa for the lower bound. For the power spectrum area used as the denominator, power is taken as the central estimate, except in the orbital band where it is taken as the upper or lower 95% confidence bound of the power spectrum. Where a ratio of precession to obliquity amplitude is reported, the upper and lower 95% intervals are approximated by dividing the upper and lower precession estimate by the central obliquity estimate.

### 3.2. Spectral estimates of orbital forcing amplitudes

We divide records into segments representing 3-2 Ma and 2-1 Ma to allow direct comparison with depth-derived records, which end at or near 2 Ma.

**Table 2**  
Amplitudes of obliquity and precession contributions from spectral and ENOF estimates. Bracketed values give approximate 95% confidence intervals, estimates are in units of  $\text{meg}^{-1}\text{ky}^{-1}$ , and bold font indicates statistical significance. Power spectral estimates reported here are equivalent to those shown in Fig. 1. ENOF estimates differ from spectral estimates in indicating significant precession contributions because ENOF estimates are associated with narrower 95% confidence intervals.

Age model	Orbitally-tuned, 3-2 Ma			
Method	Power spectrum		ENOF	
Forcing term	Obliquity	Precession	Obliquity	Precession
L2H19	<b>30.7</b> (22.9 - 42.1)	6.8 (0.0-16.8)	<b>31.0</b> (24.1-38.1)	<b>8.6</b> (3.9-14.7)
LR04	<b>24.7</b> (19.1-31.8)	2.7 (0.0-10.8)	<b>23.5</b> (18.5-28.6)	<b>7.0</b> (3.4-11.6)
DSDP 607	<b>27.2</b> (19.8 - 36.4)	6.5 (0.0-16.1)	<b>24.0</b> (18.4-30.1)	<b>8.3</b> (3.5-14.1)
ODP 677	<b>23.3</b> (12.0 - 40.3)	0.0 (0.0-22.2)	<b>21.2</b> (12.0-31.3)	3.8 (0.0-12.3)
ODP 846	<b>23.7</b> (16.8 - 33.6)	6.9 (0.0-17.1)	<b>21.5</b> (14.9-28.6)	<b>7.8</b> (2.9-14.5)
ODP 849	<b>14.6</b> (6.3 - 23.9)	5.8 (0.0-16.2)	<b>16.4</b> (9.4-23.6)	<b>5.6</b> (0.7-12.0)
ODP 980/1	<b>24.9</b> (17.0 - 35.4)	9.3 (0.0-19.7)	<b>25.0</b> (17.9-32.4)	<b>10.4</b> (5.3-17.0)

Age model	Orbitally-tuned, 2-1 Ma				Depth-derived, 2-1 Ma			
Method	Power spectrum		ENOF		Power spectrum		ENOF	
Forcing term	Obliquity	Precession	Obliquity	Precession	Obliquity	Precession	Obliquity	Precession
L2H19	<b>35.1</b> (24.1 - 52.0)	<b>24.0</b> (13.4 - 38.6)	<b>34.5</b> (24.2-45.1)	<b>22.4</b> (14.0-31.7)	<b>32.9</b> (21.6 - 49.3)	<b>23.2</b> (11.6-38.1)	<b>32.7</b> (22.2-43.2)	<b>17.6</b> (9.7-27.0)
LR04	<b>26.9</b> (20.2 - 36.2)	<b>15.8</b> (9.4 - 24.2)	<b>25.4</b> (19.2-31.9)	<b>15.8</b> (10.2-21.9)	-	-	-	-
H07	-	-	-	-	<b>26.5</b> (21.9 - 31.4)	<b>8.2</b> (2.5 - 13.9)	<b>24.0</b> (19.8-28.3)	<b>6.8</b> (4.1-10.5)
DSDP 607	<b>28.7</b> (20.5 - 39.7)	<b>20.8</b> (13.3 - 30.9)	<b>28.8</b> (22.1-36.0)	<b>19.6</b> (13.8-26.1)	<b>30.0</b> (21.1 - 41.4)	7.7 (0.0 - 19.7)	<b>28.4</b> (20.8-36.6)	<b>6.4</b> (2.3-13.4)
ODP 677	<b>27.5</b> (19.4 - 39.8)	14.2 (0.0 - 25.8)	<b>25.5</b> (16.6-34.8)	<b>16.3</b> (8.9-24.9)	<b>26.7</b> (17.7 - 40.0)	0.0 (0.0 - 15.8)	<b>24.8</b> (16.4-33.4)	<b>5.7</b> (1.3-12.6)
ODP 846	<b>25.4</b> (18.0 - 36.0)	<b>12.6</b> (2.3 - 22.3)	<b>22.6</b> (16.6-29.5)	<b>13.6</b> (7.6-20.5)	<b>27.0</b> (18.8 - 39.3)	10.0 (0.0 - 21.8)	<b>22.9</b> (17.6-28.9)	<b>9.2</b> (5.0-14.7)
ODP 849	<b>24.7</b> (17.9 - 33.4)	<b>13.8</b> (6.6 - 22.1)	<b>23.9</b> (17.9-30.3)	<b>13.7</b> (8.6-19.5)	<b>24.5</b> (17.3 - 33.5)	0.0 (0.0 - 12.4)	<b>23.0</b> (16.7-29.7)	<b>6.9</b> (2.5-13.0)
ODP 980/1	<b>19.4</b> (9.7 - 32.1)	12.2 (0.0 - 26.3)	<b>17.7</b> (8.4-28.5)	<b>10.5</b> (2.0-20.9)	<b>19.8</b> (6.0 - 34.0)	9.6 (0.0 - 25.6)	<b>18.2</b> (9.1-28.7)	<b>7.2</b> (0.4-16.8)

Spectral amplitude estimates do not rule out the possibility of significant early Pleistocene precession forcing, but substantial uncertainties preclude a confident interpretation of results. Averaged from 3-2 Ma, the estimated precession amplitude in the orbitally-tuned L2H19 is 6.8 (0.0-16.8 95% confidence interval)  $\text{meg}^{-1}\text{ky}^{-1}$ , compared with an obliquity amplitude of 30.7 (22.9-42.1)  $\text{meg}^{-1}\text{ky}^{-1}$ , giving a precession-to-obliquity amplitude ratio of 0.22 (0.00 - 0.55). Over 2 to 1 Ma, the precession amplitude averages a larger 24.0 (13.4-38.6)  $\text{meg}^{-1}\text{ky}^{-1}$  and, unlike in the previous million years, is statistically significant. A much smaller increase in the obliquity amplitude of 4.4  $\text{meg}^{-1}\text{ky}^{-1}$  is observed between the two time periods, such that the precession-to-obliquity amplitude ratio increases to 0.68 (0.38-1.10) in the later interval.

Spectral estimates in other records follow a similar pattern to L2H19 (Table 2). No records give a significant precession amplitude estimate between 3 and 2 Ma. Between 2 and 1 Ma, the presence of precession is more ambiguous, with four out of six tuned records – DSDP 607, ODP 846, ODP 849, and the LR04 stack – giving significant precession amplitude estimates. When evaluating records on the depth-derived chronology between 2 and 1 Ma, the importance of precession is even less clear, with only two records, L2H19 and the H07 stack, giving significant spectral estimates of precession.

Further ambiguity arises from precession's upper bound being poorly constrained. While only 7 of the 21 time-series evaluated give significant spectral estimates of precession, the upper 95% confidence limit on the precession estimate is greater than obliquity's lower 95% limit in four tuned records between 3 and 2 Ma, every tuned record between 2 and 1 Ma, and two records on the depth-derived timescale between 2 and 1 Ma, such that it is not always possible to rule out precession having a larger amplitude than obliquity.

It could be that Fourier-based estimation is sub-optimal for determining orbital amplitudes on account of several basic assumptions being violated. The precession signal does not appear stationary, as is implicitly assumed, with an apparently growing amplitude over the Pleistocene. Furthermore, major frequency modulations associated with precession, such as those induced by variations in eccentricity's amplitude (Burns, 1976), lend ambiguity to the energy band within which the precession signal is contained. It is also clear from Table 2 that L2H19's orbital amplitude

estimates are substantially larger than for other records over 2-1 Ma, and possible reasons for orbital amplitude differences between records are addressed in sections 4.2 and 7.1.

None of these factors necessarily explain why some records give statistically significant precession where others on the same chronology or across the same time interval do not. On one hand, we are concerned that assessing multiple records can lead to false positives and, on the other, that the high degree of variability in spectral estimates implies that the presence of significant precession cannot be ruled out. These considerations prompt our exploring a complementary method for assessing whether precession variability is present in the early Pleistocene.

#### 4. Empirical Nonlinear Orbital Fitting (ENOF)

In developing a method that is complementary to spectral analysis, we seek to utilize precession's known frequency and amplitude modulations and to allow for non-stationarity in the amplitude of the precession response over time. The method we propose below is similar to spectral analysis, which can be represented as a least-squares fit of sinusoids to a time-series (Bracewell, 1986), but modified to be a least-squares fit of the orbital elements themselves that is sequentially fit using a sliding window.

##### 4.1. Method

Previous studies have represented the orbital influence on glacial mass balance using a flexible index consisting of a weighted sum of obliquity and climatic precession (e.g. Imbrie and Imbrie, 1980), where selecting appropriate weights and climatic precession phase allows for reproducing most parameterizations of insolation forcing. Equating this index to the rate-of-change of  $\delta^{18}\text{O}$  has been shown to produce a good fit in the late Pleistocene (Imbrie and Imbrie, 1980; Roe, 2006) for the same reasons given in section 3.1. Following these previous studies, we posit a functional form for the orbital forcing of ice sheet mass balance as,

$$\frac{dV}{dt} = A_o(t)\varepsilon(t - \Delta t_o) + A_p(t)e \sin(\varpi(t - \Delta t_p)) + \eta(t). \quad (1)$$

The rate-of-change of ice volume,  $dV/dt$ , is represented as a combination of obliquity,  $\varepsilon$ , and climatic precession forcing. Climatic precession has an amplitude controlled by orbital eccentricity,  $e$ ,

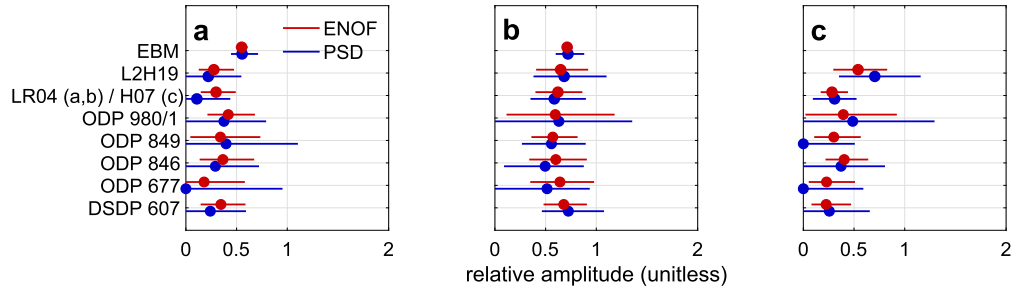


**Fig. 2.** Precession amplitude relative to obliquity in early-Pleistocene benthic  $\delta^{18}\text{O}/dt$ , as estimated by ENOF (red) and spectral analysis (blue), in (a) orbitally-tuned records for 3-2 Ma, (b) orbitally-tuned records for 2-1 Ma, and (c) depth-derived records for 2-1 Ma. Circles represent best estimates, and bars represent the 95% confidence range. Estimates from ice sheet model results described in section 6 are also included. The label for the composite records, “LR04 (a,b) / H07 (c)”, refers to the LR04 stack in panels (a) and (b), and the H07 stack in panel (c).

and phase equal to the longitude of perihelion,  $\varpi$ , taken relative to the fixed vernal equinox.  $A_p$  and  $A_o$  are the amplitudes respectively associated with obliquity and precession,  $\Delta t_o$  and  $\Delta t_p$  are the respective time offsets, and all four parameters are permitted to vary over time. Time offsets arise from age model error, the seasonal sensitivity of  $\delta^{18}\text{O}$ , and lags in the response to orbital forcing. Noise and processes not otherwise accounted for are represented by  $\eta$ . The values used for  $e$ ,  $\varpi$ , and  $\varepsilon$  are from Berger and Loutre (1991).

Taking  $\varpi$  relative to the vernal equinox gives a model in which  $\Delta t_p = 0$  implies that maximum rates of melting and ocean warming occur when perihelion aligns with Northern Hemisphere summer solstice. Initial estimates for  $A_p$ ,  $A_o$ ,  $\Delta t_p$  and  $\Delta t_o$  are all set to zero, consistent with the rate-of-change of  $\delta^{18}\text{O}$  being in phase with peak Northern Hemisphere summer intensity, but  $\Delta t_p$  and  $\Delta t_o$  could allow for precession variability of essentially any phase because they are allowed to vary within  $\pm 10$  ky. No parameter is needed for a direct offset in the precession angle  $\varpi$ , because the time offset  $\Delta t_p$  captures virtually all of the structure that such a parameter might introduce.

Values of  $A_p$ ,  $A_o$ ,  $\Delta t_p$  and  $\Delta t_o$  are estimated by a nonlinear least-squares fit of equation (1) to  $\delta^{18}\text{O}/dt$  over a box-car window of length  $\tau$  ky, centered on a time  $t$ . The rate-of-change is constructed by a first-difference of  $\delta^{18}\text{O}$  after linear interpolation to even spacing of 0.5 ky. As with spectral analysis, using a finer interpolation scheme for L2H19 only produces minor changes in estimates. Fitting is undertaken using a Matlab optimization routine which uses a trust-region algorithm for parameter estimation (see Appendix C). Before evaluation,  $\delta^{18}\text{O}/dt$  is smoothed with a 6 ky filter to minimize the influence of noise in parameter estimation. Note that smoothing a record resolved at frequencies well above that of climatic precession is expected to minimally influence orbital energy, whereas coarsely sampling a sediment core instead aliases unresolved high-frequency energy to lower frequencies (Pisias and Mix, 1988). Each window is shifted relative to the previous by  $k$  ky, and the fit repeated, until the end of the time-series is reached. Each  $t$  is therefore associated with  $\tau/k$  estimates for a parameter, which are averaged to obtain a single time-continuous estimate. Unless otherwise noted, we use  $\tau = 50$  ky and  $k = 5$  ky. Choosing  $k$  to be substantially less than  $\tau$  permits for a smooth estimate of the time-evolution of orbital amplitudes. To obtain time-averaged amplitudes for each of precession and obliquity, the square root of the variance of the first and second terms in equation (1), respectively, is taken.

Like in spectral analysis, the presence of background noise causes ENOF to overestimate orbital variance. The bias is a function of the signal-to-noise ratio (SNR), and is estimated from a Monte Carlo approach in which ENOF is run against repeated realizations of synthetic time-series containing both orbital variance and noise. The bias correction, analogous to subtracting the noise floor in spectral analysis, is made by linearly interpolating the noise frac-

tion of the total amplitude against the mean bias for that fraction, as estimated from synthetic tests (see Appendix D).

95% parameter confidence intervals for  $A_p$  and  $A_o$  are approximated under an assumption of asymptotic normality of the estimator, with further information given in Appendix C. Similarly to spectral analysis, when reporting a ratio of precession to obliquity amplitudes, the accompanying confidence interval comprises the lower and upper 95% confidence bounds for precession divided by the central obliquity estimate. Because estimates of  $\Delta t_p$  and  $\Delta t_o$  are strongly influenced by age model error and bound-constrained to avoid overfitting, confidence intervals are not expected to be informative for these parameters and are therefore not reported.

#### 4.2. Time-averaged orbital forcing amplitudes and time offsets

Unlike with spectral analysis, ENOF estimates of the precession amplitude in L2H19 are significant throughout the full 3-1 Ma period. Between 3 and 2 Ma, ENOF gives a precession amplitude of 8.6 (3.9-14.7)  $\text{meg}^{-1}\text{ky}^{-1}$  and an obliquity amplitude of 31.0 (24.1-38.1)  $\text{meg}^{-1}\text{ky}^{-1}$ , which together yield a precession-to-obliquity ratio of 0.28 (0.13-0.47). The precession estimate rises to 22.4 (14.0-31.7) between 2 and 1 Ma, whereas the obliquity amplitude increases by only 3.5  $\text{meg}^{-1}\text{ky}^{-1}$ , such that their ratio rises to 0.65 (0.41-0.92) between 2 and 1 Ma (Table 2).

The apparent detection of significant precession in the 3-2 Ma interval is supported by ENOF estimates in other records, with all but one orbitally-tuned record giving significant precession estimates over this time period (Table 2). Confidence in the significance of precession in the early Pleistocene is bolstered by a finding that ENOF precession estimates are significant in every record on both the orbitally-tuned and depth-derived chronologies between 2 and 1 Ma. Note, however, that central estimates of the precession-to-obliquity amplitude ratio average 50% lower in depth-derived records relative to orbitally-tuned records (Fig. 2b,c). Differences in precession estimates between age models is further discussed in section 7.1.

As is the case with spectral analysis, L2H19 features significantly larger orbital amplitudes than other records (see Table 2). More generally, orbital amplitudes are systematically higher in North Atlantic records than in Pacific records, and this may partly reflect greater variance from deep-water temperature in North Atlantic benthic  $\delta^{18}\text{O}$  records (Duplessy et al., 1980; Waelbroeck et al., 2002). There does not appear to be a substantial difference in the relative sensitivity to precession versus obliquity between basins, with the ratio between the two averaging 0.64 for North Atlantic and 0.60 for Eastern Pacific orbitally-tuned records between 2 and 1 Ma.

The estimated time offsets,  $\Delta t_p$  and  $\Delta t_o$ , serve to quantify the timing of orbitally-induced variations in  $\delta^{18}\text{O}$ . Several factors make it unwise to place much weight on individual time offset estimates,

however, including that (i) age uncertainties are up to half the period of precession (Huybers, 2007), (ii) there remains significant uncertainty regarding what controls the precession phase in global climate records (e.g. Kawamura et al., 2007), (iii) orbitally-tuned records have previously been aligned to a Northern Hemisphere ice-volume curve, and (iv) the ENOF model is centered about a Northern Hemisphere summer forcing. Despite these factors, agreement across several records and age models would provide confidence that the estimated precession variability represents a consistent set of physical processes.

Mean  $\Delta t_p$  is no more than  $\pm 1$  ky in records on both age models and over both 3–2 Ma and 2–1 Ma. In orbitally-tuned records,  $\Delta t_p$  averages -0.2 ky between 3 and 2 Ma, and 0.1 ky between 2 and 1 Ma, and in depth-derived records,  $\Delta t_p$  averages 0.5 ky between 2 and 1 Ma. Similarly, mean  $\Delta t_o$  does not exceed 3 ky in any record on either age model, averaging 0.5 ky over 3–2 Ma and 1.6 ky over 2–1 Ma in orbitally-tuned records, and 2.4 ky over 2–1 Ma in depth-derived records. Given age uncertainties of  $\pm 6$  ky for tuned records (Lisiecki and Raymo, 2005) and  $\pm 10$  ky for depth-derived records (Huybers, 2007),  $\Delta t_p$  and  $\Delta t_o$  in  $\delta^{18}\text{O}/dt$  may be interpreted as being indistinguishable from in-phase with the intensity of Northern Hemisphere summer.

The algorithm may occasionally fail to adequately search the parameter space, returning a  $\Delta t_p$  value equal to its initial estimate, though this may also occur if the initial estimate is optimal. Excluding values of  $\Delta t_p$  that are equal to the initial estimate before averaging does not lead to qualitatively different results, with all records giving a mean  $\Delta t_p$  of less than 2 ky and a mean  $\Delta t_o$  less than 3.5 ky.

## 5. Detailed analysis of orbital forcing in L2H19

An analysis of the temporal variability and trends in the estimated precession component of benthic  $\delta^{18}\text{O}$  further informs the physical origin of the signal and whether it can confidently be attributed to precession forcing. Of the records we have evaluated, L2H19 has the highest sampling resolution by a wide margin (Table 1) and features high sedimentation rates through the Pleistocene (Channell et al., 2016; Hodell and Channell, 2016). In light of these exceptional properties, we are motivated to more closely evaluate Pleistocene precession variability using L2H19.

### 5.1. Further evidence for precession forcing in early Pleistocene benthic $\delta^{18}\text{O}$

A common method for testing whether precession-band variance in a  $\delta^{18}\text{O}$  record is of physical origin is to pass the record through a narrow band-pass filter admitting only precession frequencies, typically  $1/18 \text{ ky}^{-1}$  to  $1/24 \text{ ky}^{-1}$ , and measure the correlation of the filtered signal's amplitude with that of eccentricity (e.g. Shackleton et al., 1990). Filtering can produce eccentricity-like amplitude modulations in orbitally-tuned records even when no relationship with eccentricity exists (Huybers and Aharonson, 2010), though methods have been proposed to overcome this problem. Zeeden et al. (2015) suggested that filtering records using a wider band, e.g.  $1/8$  to  $1/35 \text{ ky}^{-1}$ , then calculating the instantaneous amplitude of the filtered time-series using the Hilbert transform and smoothing the resulting curve permits for avoiding spurious detections of eccentricity modulation. ENOF offers a simpler alternative. Undertaken fully in the time domain, ENOF does not require filtering a record to identify amplitude variability, thereby avoiding the primary concern raised by Huybers and Aharonson (2010).

If ENOF is repeated with eccentricity excluded from the climatic precession term of equation (1),  $A_p$  is responsible for capturing all amplitude modulations of precession. The correlation of  $A_p$  with

eccentricity then provides an independent test for the presence of precession. Because ENOF can only resolve variations on timescales equal to or longer than the length of its fitting window, here 50 ky, eccentricity is smoothed by a window of the same length prior to computing the correlation.

The correlation of  $A_p$  with eccentricity in the orbitally-tuned L2H19 between 3 and 1 Ma is 0.46. The significance of this correlation is evaluated against a null hypothesis,  $H_{0, ecc}$ , that  $A_p$  varies independently of eccentricity. A probability distribution associated with  $H_{0, ecc}$  is formed by repeating the eccentricity-independent fit  $10^4$  times on phase-randomized versions of the input data (Schreiber and Schmitz, 2000). Phase randomization preserves the Fourier amplitudes and power spectrum of the time-series, but destroys meaningful amplitude modulations. The 99% significance level for  $H_{0, ecc}$  is found to be 0.38, allowing for a conclusion that the eccentricity modulation in L2H19 is highly significant. Variations in the window width or window shift ( $\tau$  or  $k$ , respectively, in section 4) only induce small variations in the correlation between eccentricity and  $A_p$  (Appendix C.2). Repeating the test with a 100-ky ENOF fitting window gives an equally significant result.

### 5.2. Trends in forcing amplitudes

Previous work has generally described the Pleistocene as involving a distinct transition between a “41-kyr world”, featuring apparently obliquity-dominated glacial cycles, and the later “100-kyr world”, with more strongly expressed precession (e.g. Elderfield et al., 2012). Some studies have alternately described a more gradual progression in glacial-cycle characteristics (Huybers, 2007; Lisiecki and Raymo, 2007). An ENOF fit using a 100-ky window over the past 3 Ma indicates that precession's contribution to L2H19's  $\delta^{18}\text{O}/dt$  rose over the Pleistocene with no abrupt transition (Fig. 3c). Precession's amplitude increased at a rate of  $(16.21 \pm 0.42) \times 10^{-3} \text{ meg}^{-1} \text{ ky}^{-2}$  between 3 Ma and the present, more than five times faster than the growth rate in obliquity amplitude,  $(2.82 \pm 0.29) \times 10^{-3} \text{ meg}^{-1} \text{ ky}^{-2}$  (Fig. 3). These results accord with an earlier finding that the spectral power of precession-band frequencies in  $\delta^{18}\text{O}$  increases in amplitude over the Pleistocene (Lisiecki and Raymo, 2007). Note that eccentricity itself has slightly larger amplitude on average in the late Pleistocene, but recomputing the precession amplitude trend using a linearly de-trended eccentricity negligibly changes the result.

The residual between the ENOF fit and  $\delta^{18}\text{O}/dt$  gradually increases between 3 and 1 Ma, a trend that can largely be explained by an increase in the variance of  $\delta^{18}\text{O}/dt$  over the same interval. A linear regression between the moving variance of  $\delta^{18}\text{O}/dt$  and the moving variance of the ENOF residual using a box-car window of 250 ky yields an  $R^2$  of 0.91. Additional amplitude variability is superimposed upon precession's amplitude trend due to its modulation by eccentricity, as can be recognized in the time domain. For example, the peak at 1.75 Ma in Fig. 3a apparently corresponds to a strong precession peak during an eccentricity maximum.

## 6. Predictions of an ice sheet and energy-balance model

To examine a possible physical explanation for the observed orbital ratios in benthic  $\delta^{18}\text{O}$  records and the gradual increase in precession amplitude relative to obliquity, we revisit the coupled Northern Hemisphere ice sheet and energy-balance model of Huybers and Tziperman (2008), hereafter the EBM. The EBM represents a parabolic ice sheet in a two-dimensional transect from the equator to the North Pole, and is forced with diurnally averaged daily insolation across all latitudes, permitting it to capture the full seasonal temperature cycle. The model computes heat fluxes across a two-layer atmosphere and a subsurface layer, with an ice sheet

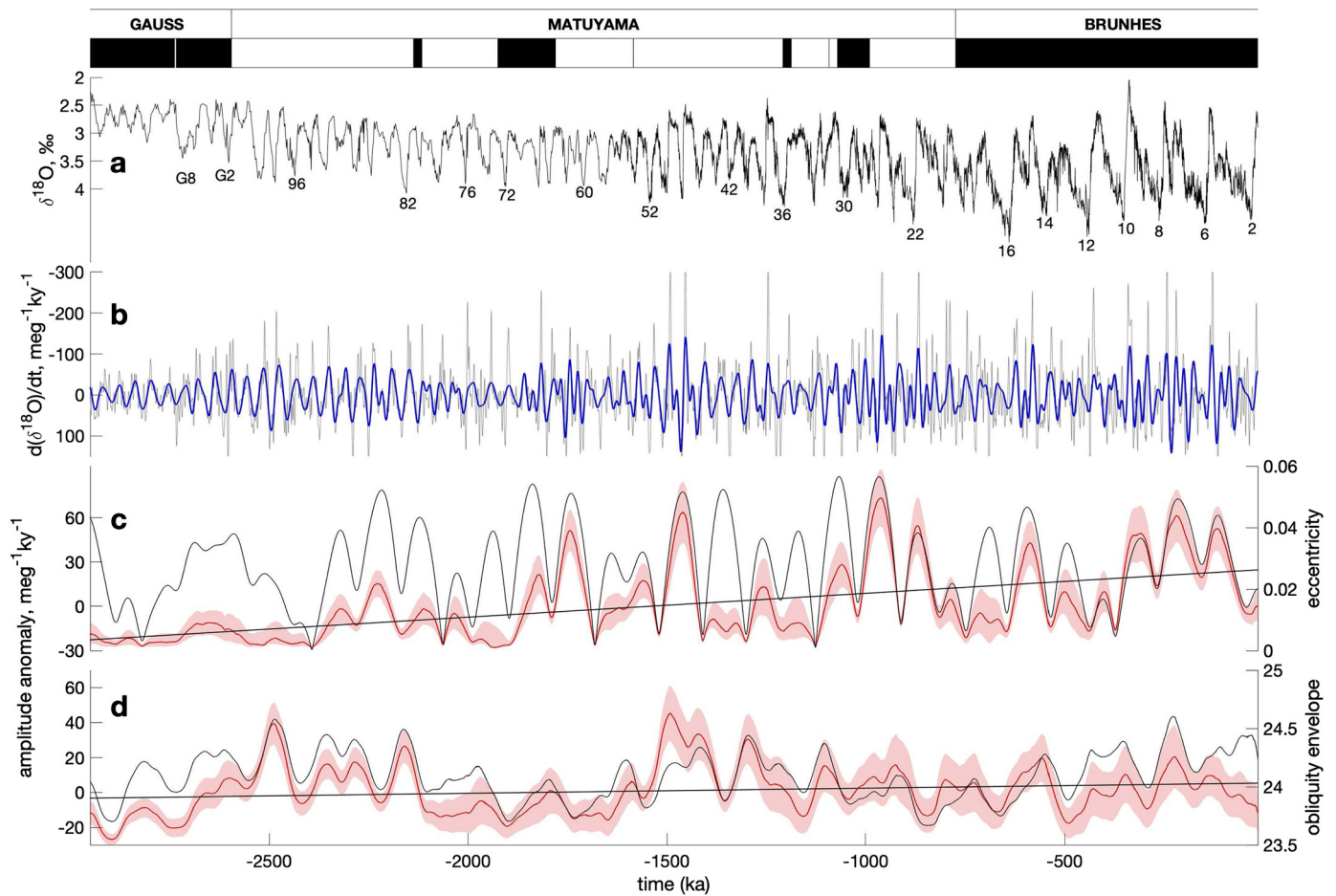


**Fig. 3.** Trends in orbital forcing in  $\delta^{18}\text{O}/dt$  owing to precession and obliquity over the Pleistocene and late Pliocene using data from L2H19, a high-resolution benthic  $\delta^{18}\text{O}$  record. **(a)** L2H19, with select Marine Isotope Stages labeled, and its geomagnetic polarity reversal stratigraphy (Channell et al., 2008, 2016). **(b)** The rate-of-change of  $\delta^{18}\text{O}$  smoothed with a 6 ky 2nd-order Butterworth filter (gray), and ENOF fit to the time-series (blue) **(c)** Envelope of the precession contribution from 3 to 0 Ma (red line) and orbital eccentricity (black line). **(d)** same as (c), but for obliquity, and where the black line represents the envelope of obliquity. Envelopes are calculated as the magnitude of the Hilbert transform of the ENOF-estimated precession and obliquity contributions, as well as for the astronomically calculated values for obliquity. Shaded areas represent the 95% confidence intervals, and black trend-lines indicate a linear least-squares fit. The ENOF fit uses a 100 ky window, but results are similar when using a 50 ky window (see Fig. C.2). The y-axis is reversed in panels (a) and (b).

that freely deforms in accordance with a shallow-ice approximation and sits above a deformable sediment layer.

A number of important factors are not included. There is no ocean, and the model does not simulate geochemical interactions such as those that may drive a  $\text{CO}_2$  feedback (Broecker, 1982), nor the possible influence of sea ice (Gildor and Tziperman, 2000) or orbitally-forced fluctuations in the volume of the Antarctic ice sheet (Raymo et al., 2006). Though these limitations are important to note, the model has been shown to produce ice-volume variability that was previously interpreted to contain little precession (Huybers and Tziperman, 2008), allowing us to evaluate the EBM output in the same context as the observations.

### 6.1. Orbital forcing in a two-million year model run with a cooling atmosphere

We analyze a single run of the EBM starting at 3.1 Ma, the first 100 ky of which is excluded from analysis as an initialization period (Fig. 4), using the parameters listed in Tables E.3 and E.4. A cooling of the background climate is imposed for consistency with an observed long-term cooling trend. To impose this cooling, the height of the atmospheric radiation emission level is linearly lowered from 7.20 km to 7.06 km between 3.1 and 1 Ma, which cools the Northern Hemisphere surface temperature by  $2.2^\circ\text{C}$ . Cooling averaged between  $45^\circ\text{N}$  and  $70^\circ\text{N}$  is  $2.7^\circ\text{C}$ , consistent with an es-

timated North Atlantic sea-surface-temperature cooling of  $2.8^\circ\text{C}$  over 3 to 1 Ma (Lawrence et al., 2010).

Orbital forcing amplitudes are estimated from differenced ice volume, and only ENOF results are reported because spectral analysis produces very similar central estimates, giving precession-to-obliquity amplitude ratios within 0.01 of those estimated from ENOF. Averaged over 3–2 Ma, ENOF estimates a precession-to-obliquity amplitude ratio of 0.55 (0.49–0.61 95% confidence interval) in simulated ice volume. This ratio exceeds that estimated in the observations, which average 0.32. The ratio grows to 0.71 (0.68–0.75) between 2 and 1 Ma, a shift caused almost entirely by an increase in the precession contribution. During this later interval, the partitioning of orbital energy in the EBM is consistent with orbitally-tuned records in which the ratio averages 0.62 (see Fig. 4 for a comparison of L2H19 against simulated ice volume).

The upward trend in the model ice volume's precession amplitude can be understood as an ice sheet's response to gradually cooling atmospheric temperatures. Cooling reduces melting both because of a shorter melt season and less intense melting therein, leading to growth of the ice sheet and a southward shift of the ablation margin. Both a shorter melt season and a more southerly melting line will lead to greater precession variability (see Huybers and Tziperman (2008) and sensitivity tests in Fig. E.1), where the former heightens the sensitivity to summer intensity, and the lat-

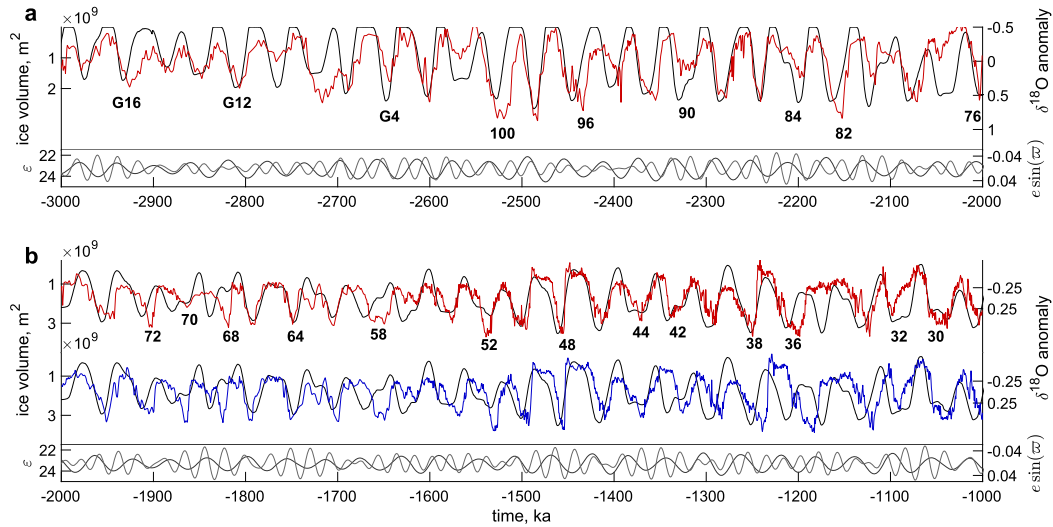


**Fig. 4.** Simulated variations in ice volume between 3 and 1 Ma. **(a)** Model ice volume (black) and L2H19 on an orbitally-tuned age scale (red) for 3–2 Ma. Variations in obliquity (black) and the climatic precession parameter ( $e \sin(\varpi)$ , light gray) are below. **(b)** Similar to (a) but for 2–1 Ma and with L2H19 also shown on a depth-derived age scale (blue).  $\delta^{18}\text{O}$  values are de-trended over each 1 Ma segment. Select Marine Isotope Stages are labeled for reference.

ter exposes the melting line to long-term insolation variations that are more strongly influenced by precession.

Following past approaches (Raymo and Nisancioglu, 2003; Raymo et al., 2006), we have treated  $\delta^{18}\text{O}$  as being indicative of ice volume, though it is also sensitive to the local deep-water temperature. Previous efforts to deconvolve benthic  $\delta^{18}\text{O}$  into its respective components have used an inverse model of an ice sheet coupled to a simplified representation of deep-water temperature (e.g. Bintanja and van de Wal, 2008) or empirical isolation of the temperature component from independent measurements of calcite Mg/Ca ratios (e.g. Elderfield et al., 2012). There remain large uncertainties in the relative amplitudes of ice volume and deep-water temperature in benthic  $\delta^{18}\text{O}$  (Bintanja et al., 2005), however, making it difficult to produce a pure ice-volume curve from which to directly estimate orbital forcing. The phase of precession in any such deconvolution is also uncertain because it is sensitive to factors including the lag in the response to orbital forcing, amplitude of Southern Hemisphere contributions, and seasonal sensitivity of the deep-water temperature component, each of which is uncertain.

## 7. Discussion and conclusions

### 7.1. Differences in precession estimates across records and methods

The detection and interpretation of orbital variability in climate proxies would be straightforward if orbital variations were unmodulated sinusoids, records were sampled at high resolution, sedimentation rates were stable across space and time, and noise and nonlinearity were small. Clearly, orbitally-induced changes in radiative forcing and the subsequent proxy recording of the response are not so simple. It is therefore unsurprising that various proxy records have engendered different interpretations when evaluated with different methods, on different chronologies, or compared against different physical models.

Spectral analysis detects significant precession in just 7 out of the 21 samples across records, evaluated on two different 1 Ma intervals, and with two different age models (Table 2). In contrast, ENOF identifies a significant precession contribution in 20 out of 21 samples. The higher rates of detection with ENOF corresponds with the algorithm producing 95% confidence intervals that are, on average, 30% narrower than for spectral estimates. Higher detection rates are only physically meaningful, however, if they are

not borne of an increased probability of false detection. Thus, a series of tests on synthetic time series are undertaken to explore differences between ENOF and spectral analysis. These tests are described in Appendix D and briefly summarized here. Synthetic signals are formulated by adding background noise similar to that found in the observations (Fig. 1) with obliquity and climatic precession signals. The relative skill of ENOF versus spectral analysis depends on the amplitude of the orbital signal relative to noise, and in the case of a high signal-to-noise ratio, there is negligible difference between the two methods' skill (Figs. D.1 and D.2), as found in analysis of the EBM's simulated ice volume in section 6.

Signal-to-noise ratios are estimated for observations by dividing the total energy above the noise floor in both orbital bands by the sum of all other energy in the power spectrum, giving an average of 0.20 and ranging from 0.03 to 0.35 across the 21 different samples. The one exception is the H07 stack for which the signal-to-noise ratio is 0.92, possibly because noise is suppressed through averaging multiple records. Note that because obliquity has a larger amplitude than precession, the signal-to-noise ratio for each orbital component differs, but we do not account for this distinction. For a signal-to-noise ratio of 0.075, our synthetic results indicate that the 95% coverage interval associated with ENOF is 36% narrower than for spectral estimates, and for a signal-to-noise ratio of 0.25 the range is 26% narrower. These empirical coverage intervals are thus consistent with the 30% narrower confidence intervals determined for ENOF relative to spectral analysis (Table 2) and with ENOF having greater statistical power for identifying climatic precession.

In contrast to its better identifying orbital variations in the presence of noise, ENOF is relatively more sensitive to age model errors than our spectral analysis approach (Fig. D.3). Greater sensitivity can be understood in that ENOF fits only to a specific time-series of orbital forcing, whereas spectral estimates are insensitive to phase shifts, and our approach of summing orbital energy across a frequency band permits for recovering energy dispersed from the exact frequencies associated with orbital variations. This accords with ENOF giving lower central estimates of precession amplitudes than spectral analysis in all but two depth-derived records (Table 2).

Estimates of the amplitude of obliquity variability are less sensitive to age model errors than precession on account of its longer period leading to smaller phase differences for a given perturbation in time (Fig. D.3). This difference in sensitivity makes it

useful to consider the ratio of precession to obliquity variability in records, but we find a surprisingly large difference in these ratios when transitioning from orbitally-tuned to depth-derived age models. Estimates of precession-to-obliquity amplitude ratios in depth-derived records average 50% lower than for orbitally-tuned records if using ENOF and 58% lower if using spectral analysis. Age errors having a standard deviation between 2 and 5 ky are only expected to decrease the precession amplitude by an average of <1% to 28% (Fig. D.3). Age errors having a standard deviation of 10 ky is required for a >50% reduction in precession amplitude, but then a large decrease in the amplitude of obliquity is also anticipated. We speculate that orbital tuning accounts for a portion of the otherwise larger-than-expected decrease in orbital energy. The first step of orbital tuning for records included in the LR04 stack involves mapping  $\delta^{18}\text{O}$  variations onto a curve representing simulated ice-volume from a model forced with June 21 insolation at 65°N (Lisiecki and Raymo, 2005; Imbrie and Imbrie, 1980), which primarily contains climatic precession variability. Tuning  $\delta^{18}\text{O}$  records to a precession target using a dynamic time warping algorithm similar to that involved in the LR04 alignment procedure has been shown to artificially increase estimates of the precession amplitude (Proistosescu et al., 2012). The combination of depth-derived ages being untuned and their containing age errors may account for estimates of precession amplitude being much smaller when using depth-derived as opposed to orbitally-tuned ages.

A final consideration for differences in orbital amplitudes relates to variable sampling resolution across records. Coarsely sampling marine sediment records aliases high-frequency variability into lower-frequency bands (Pisias and Mix, 1988). Moreover, sampling intervals above the Nyquist frequency may not suffice for fully resolving orbital variability because of uneven sampling, time uncertainty, and the amplitude and frequency modulation present in obliquity and climatic precession. Between 2 and 1 Ma, the sampling resolution in depth-derived records varies by more than an order of magnitude, with L2H19 averaging 60 data points over a 21 ky precession cycle, and DSDP 607 averaging just 5.5 points. If L2H19 were resampled at a resolution equal to that of the DSDP 607 record, a 16% lower precession amplitude estimate would be expected from either ENOF or spectral analysis, compared to an essentially unchanged estimate of the obliquity amplitude (Fig. D.5). Although possibly only a coincidence, the DSDP 607 estimate of the amplitude of precession using the orbitally-tuned age model is, in fact, 15% lower than for L2H19, where both records are from the North Atlantic and obtained at similar water depths.

## 7.2. Interpretation of orbital amplitudes and trends

Despite some evidence for the presence of precession in early Pleistocene glacial cycles (e.g. Lisiecki and Raymo, 2007), a long-standing view has persisted that precession variability in early Pleistocene benthic  $\delta^{18}\text{O}$  is mostly negligible in amplitude (Rudiman et al., 1986), motivating explanations for obliquity-paced glacial cycles (Raymo and Nisancioglu, 2003; Loutre et al., 2004; Raymo et al., 2006; Huybers, 2006; Tabor et al., 2015). Our finding that early Pleistocene  $\delta^{18}\text{O}$  records contain significant precession variability nearly in phase with Northern Hemisphere summer intensity suggests that proposed mechanisms to continuously suppress precession may be less relevant to the early Pleistocene than previously believed.

One possibility is that, in accordance with classical Milankovitch theory, glaciation is controlled by Northern Hemisphere summer insolation (Milankovitch, 1941; Huybers, 2006). In such a model, the observed gradual increase in precession amplitude (Fig. 2) is explained on the basis of a southward extension of the ice sheet ablation margin induced by global cooling, making variations in ice volume more sensitive to precession. An alternative interpretation,

consistent with the proposal of Murphy (1869), is that the early Pleistocene represents a transitional period in which the net precession contribution to global ice volume shifts from Southern to Northern Hemisphere dominance. Such a model also holds global cooling responsible for the increase in precession amplitude, but instead implies that anti-phased precession-forced ice volume fluctuations between hemispheres, which would cause cancellation of the  $\delta^{18}\text{O}$  precession signal (Raymo et al., 2006), became increasingly imbalanced from Northern Hemisphere ice sheets growing in size and, possibly, Antarctica becoming more stable.

Neither model excludes the possible importance of other factors. For example, erosion of regolith by an ice sheet (Clark and Pollard, 1998) could contribute to thicker ice sheets whose ablation zones are relatively further south and, therefore, exposed to greater precession variability in local insolation. Past efforts to model the ice sheet response to real or idealized orbital forcing have yielded ice volume fluctuations ranging from precession-dominant (e.g. Nisancioglu, 2004) to obliquity-dominant (e.g. Berger et al., 1999). The variety in these results as well as the possible importance of mechanisms not included in the EBM suggests a need for further empirical analyses and simulation to better determine the characteristics of early-Pleistocene glacial variability and its causes.

Two further important questions have not been explored here. First, the origin of glacial cycle asymmetry, which has been identified throughout the full Pleistocene (Ashkenazy and Tziperman, 2004; Lisiecki and Raymo, 2007), remains uncertain, and further exploration of the connections between precession forcing, asymmetry, and age model accuracy would be useful. Second, it has been suggested that both the phase and amplitude of Pleistocene 100-ky variability are sensitive to precession (e.g. Imbrie et al., 1993). Lisiecki (2010) proposed that strong precession forcing disrupts 100-ky variability in  $\delta^{18}\text{O}$  over the past 5 Ma, but raised the question of “how precession modulation could suppress 100-kyr glacial cycles during the early Pleistocene ‘41-kyr world’ when the 23-kyr power of  $\delta^{18}\text{O}$  is negligible”. Caballero-Gill et al. (2019) suggested that 100-kyr glaciations also occurred during the Pliocene and proposed that a nonlinear response to precession is responsible. Our finding of significant early-Pleistocene precession variability suggests that further investigation into the links between orbital eccentricity, precession forcing, and quasi-100-ky climate variability is needed.

A revised description of the early Pleistocene as featuring significant and gradually increasing precession amplitude in phase with Northern Hemisphere summer intensity recasts the time period as supporting, rather than contradicting, the long tradition of models that invoke changes in summer insolation as controlling global ice volume fluctuations (Murphy, 1869; Milankovitch, 1941; Hays et al., 1976; Imbrie and Imbrie, 1980; Raymo et al., 2006). Whether the early Pleistocene accords more readily with the model of Milankovitch or that of Murphy remains to be seen.

## Declaration of competing interest

The authors declare that they have no known competing financial interests or personal relationships that could have appeared to influence the work reported in this paper.

## Acknowledgements

PRL and PJH were supported by National Science Foundation award 1338832. DAH was supported by Natural Environment Research Council grant NE/R000204/1 and Engineering and Physical Sciences Research Council grant EP/S030417/1. DAH thanks D. Schrag and the Harvard University Center for the Environment for supporting a sabbatical during AY 2018-2019. This research

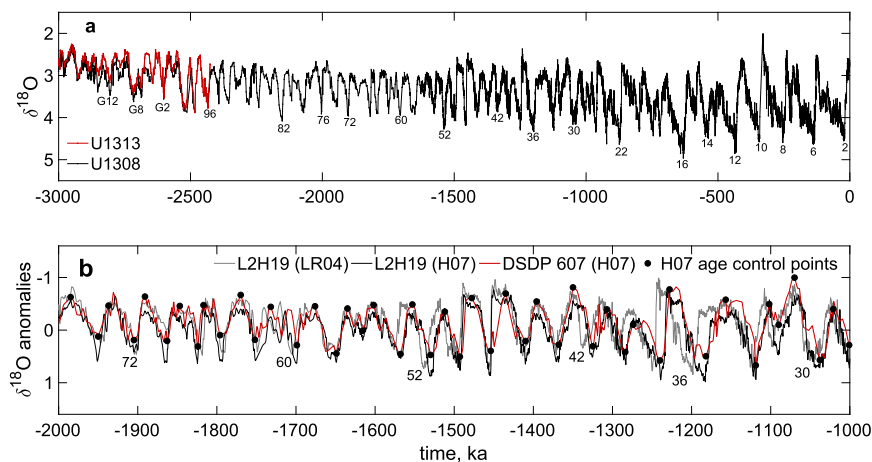


**Fig. A.1.** Pleistocene  $\delta^{18}\text{O}$  records and age models for L2H19. (a) The orbitally-tuned L2H19 benthic  $\delta^{18}\text{O}$  record comprising data from IODP Sites U1313 (red) and U1308 (black). (b) L2H19 (black) after alignment to a depth-derived timescale for DSDP 607 (red), where black markers are age control points used for calibration. The orbitally-tuned L2H19 is also shown (gray) for comparison. Records in panel (b) are de-trended to enable direct comparison, and select Marine Isotope Stages are labeled in both panels.

used data provided by the International Ocean Discovery Program (IODP).

### Appendix A. Depth-age relationships

Orbitally-tuned chronologies are developed by matching to LR04. The LR04 age model is constructed by alignment of the LR04 stack with the ice-volume model of Imbrie and Imbrie (1980), where ice-model parameters are adjusted over time to give an increasingly asymmetric target and longer response time owing to larger ice sheets. Tuning is achieved first by maximizing the correlation between the stack and ice model, then further adjusting the timescale to be in phase with the ice model's obliquity component. The re-tuning to obliquity allows the precession phase to vary between glacial cycles. The depth-derived approach uses the orbitally-independent age model of Huybers (2007), referred to as H07. H07 is constructed by graphic correlation of 14 benthic and planktic records and alignment of synchronous geomagnetic and isotopic events across records, between which age is linearly interpolated with depth after correcting for downcore compaction.

L2H19's orbitally-tuned chronology is based on alignment to the LR04 stack by identification of isotopic events occurring both in LR04 and L2H19, with an assumption of linear sedimentation rates between the aligned isotopic events (Bolton et al., 2010; Channell et al., 2016; Hodell and Channell, 2016). The age model is supplemented by correlation of sediment lightness to ODP Site 609 between the present and 76 ka and to the NGRIP record between 76 and 110.5 ka (Hodell and Channell, 2016).

To convert L2H19 to a depth-derived timescale, it is aligned with the benthic  $\delta^{18}\text{O}$  record of Site 607 on the H07 age model. Site 607 is chosen because it is closest geographically to the records comprising L2H19, being drilled at the same location as U1313 in the North Atlantic, and is therefore likely to have the most similar glacial cycles. Note, however, that the H07 age model for Site 607 is based on a global calibration with other records in the H07 stack. Isotopic event ages used in calibrating H07 are adopted as age control points (ACPs) for L2H19, with a total of 48 events identified between 2 and 1 Ma. The ACPs of L2H19 and Site 607 are aligned by assigning to L2H19's ACPs the ages of Site 607's ACPs, then linearly interpolating age with depth between these points. The depth-derived timescale ends at 2 Ma because too few independent  $\delta^{18}\text{O}$  records exist beyond 2 Ma to adequately constrain age-depth relationships without orbital assumptions. The five other individual records included in this study are also eval-

uated on both orbitally-tuned and depth-derived age scales, following the age models of LR04 and H07, respectively. They are used here as published in Lisiecki and Raymo (2005) and Huybers (2007).

### Appendix B. Spectral estimates

All power spectra are computed with Thomson's multi-taper method (Percival and Walden, 1993) using three tapers. The noise floor for the power spectrum is computed by a least-squares fit of a power-law,

$$y = Af^q, \quad (\text{B.1})$$

to the power spectrum, where the parameters  $A$  and  $q$  are chosen to minimize the sum of squared residuals between  $y$  and the power spectrum. Frequencies below  $1/150 \text{ ky}^{-1}$ , between  $1/41 \pm 1/125$ , between  $1/21 \pm 1/125$ , and above  $1/5 \text{ ky}^{-1}$  are excluded from the fit. If the net spectral energy in a band is negative with respect to the estimated noise floor, the amplitude is assigned a value of zero. The noise floor is approximately white in the rate-of-change of  $\delta^{18}\text{O}$  (Fig. 1). Across all records on both the orbitally-tuned and depth-derived age models and both time intervals evaluated (3–2 Ma and 2–1 Ma),  $A$  averages  $0.02 \pm 0.02$  and  $q$  averages  $-0.01 \pm 0.2$ , where the interval represents one standard deviation.

The 95% confidence interval for power spectral density is estimated from the approximate  $\chi^2$  distribution of the spectral estimator (Percival and Walden, 1993). The interval is given by  $\left[ \frac{\nu S(f)}{Q_\nu(p)}, \frac{\nu S(f)}{Q_\nu(1-p)} \right]$ , where  $S$  is the estimate at frequency  $f$ ,  $\nu$  is the equivalent degrees of freedom, and  $Q_\nu(p)$  and  $Q_\nu(1-p)$  are the  $p = 0.025$  and  $1 - p = 0.975$  percentage points on the  $\chi_\nu^2$  distribution with  $\nu$  degrees of freedom. For an estimate at a given frequency,  $\nu$  is approximately equal to  $2K$  where  $K$  is the number of tapers used in the multi-taper analysis. The overall orbital amplitude estimate has more degrees of freedom, however, because it is obtained by summing energy across several spectral estimates in an orbital band. There are  $B_f/B_W$  independent spectral estimates in an orbital band, where  $B_f = 2/125 \text{ ky}^{-1}$  is the width of an orbital band and  $B_W$  is the spectral bandwidth, which represents the frequency range across which spectral estimates decorrelate. An orbital amplitude estimate therefore has approximately  $\frac{2KB_f}{B_W}$  degrees of freedom.

Several aspects of the confidence interval for spectral estimates are uncertain. A simple power-law representation of the noise floor, equation (B.1), is assumed, and its coefficients are influenced by the choice of frequency range over which it is fit, here 1/150 to 1/5  $\text{ky}^{-1}$ . The variance of the spectral estimator is not perfectly  $\chi^2$ -distributed when deterministic variance is partially responsible for the spectral peak, as the  $\chi^2$  approximation is most accurate for a random process (Percival and Walden, 1993). To check the applicability of the approximate confidence intervals for the purposes of this study, we compute the fraction of synthetic tests, described in Appendix D, for which the true precession amplitude lies within the confidence interval. For tests with SNR=0 (pure noise), 0.075, 0.25, 0.5, 1, and 2, the estimated confidence interval contains the true amplitude in 93.8%, 97.3%, 98.5%, 99.7%, 99.99% and 100% of tests after bias correction, implying the coverage is approximately correct for noisy signals and conservative for less noisy signals. The average approximate SNR of 0.20 in observations implies that the coverage interval is expected to be generally appropriate and in some cases slightly conservative. Note that for SNR<1, the confidence interval is less conservative than for ENOF (see D.1), suggesting that the relative uncertainty of spectral analysis is not being overstated in our comparison of methods.

An alternative method for estimating uncertainties is to evaluate the significance of orbital-band spectral energy relative to the expected distribution of the null hypothesis of no orbital energy. In this approach, an approximate  $\chi^2$  confidence interval is constructed for the position of the noise floor, and an orbital amplitude estimate is considered significant if the integrated energy between the power spectral density and the 95% level for the noise floor in an orbital band exceeds zero. We elect not to use this approach because it does not provide an estimate of the uncertainty range associated with the orbital amplitude estimate, only providing a measure of the estimate's statistical significance. It is nonetheless useful to verify that the use of the alternative method wouldn't lead us to different conclusions. Repeating the analysis with this method gives no significant precession amplitude estimates among orbitally-tuned records between 3 and 2 Ma, four significant estimates for tuned records between 2 and 1 Ma, and one significant estimate for depth-derived records between 2 and 1 Ma, similar to the zero, five, and two significant estimates, respectively, from the method we use. The slightly more conservative results in the alternative method arises from the fact that the  $\chi^2$  distribution is asymmetric, so that the difference between its 2.5th and 50th percentile is less than between its 50th and 97.5th percentile. Because confidence is assessed on the basis of an upper confidence level for the noise floor in the alternative method and a lower confidence level for the power spectrum in the method we use, the latter will tend to indicate significance more often. In our case, results from both methods are similar because the summed orbital energy estimates contain approximately 24 degrees of freedom, making the resulting  $\chi^2$  distribution close to symmetric.

### Appendix C. Empirical Nonlinear Orbital Fitting (ENOF) algorithm

The parameter search for  $A_p$ ,  $A_o$ ,  $\Delta t_p$  and  $\Delta t_o$  in ENOF is undertaken using a Matlab routine, "lsqcurvefit", which uses a trust-region algorithm for optimization. The trust-region method is preferred over a Levenberg-Marquardt method because it allows us to place bound constraints on the parameter values.  $\Delta t_o$  and  $\Delta t_p$  are capped at  $\pm 10$  ky to avoid overfitting. Initial estimates are set at 0 for all parameters.

Being a gradient-descent method, the trust-region algorithm is not a global search of all possible parameter combinations so does not theoretically guarantee a global minimum. Such an exhaustive search is computationally prohibitive. Nonetheless, it is useful to

check that the parameter space is likely smooth and without multiple local minima that could cause a gradient-descent method to converge to the wrong values. A "brute force" parameter search on a select 50 ky window reveals a smooth, elliptical parameter space with respect to the residuals, and converges toward the parameter values selected by nonlinear least squares (Fig. C.1).

#### C.1. Parameter uncertainties and confidence intervals

The 95% confidence intervals for  $A_p$  and  $A_o$  are estimated using the Matlab routine "nlparci". They are approximated from a linearization of the nonlinear regression problem under an assumption that the estimator is asymptotically normally distributed. The approximate confidence interval is given by  $\hat{\theta}_{CI} = \hat{\theta} \pm S_E T_{inv}(1 - \alpha/2, n - p)$ , where  $\hat{\theta}$  is the vector of nonlinear regression parameter estimates.  $S_E$  is the estimated standard error, and  $T_{inv}$  the Student's T inverse cumulative distribution that is evaluated at a confidence level  $\alpha$  with degrees of freedom equal to the number of observations,  $n$ , minus the number of model parameters,

$p$ . Here,  $S_E(\hat{\theta}_i) = s \|r^i\|$ , where  $s = \sqrt{\frac{SSR(\hat{\theta})}{n-p}}$ .  $SSR$  is the sum of squared residuals, and  $r^i$  is the  $i$ th row of the matrix  $R^{-1}$ , which originates from a  $QR$ -factorization of the Jacobian matrix,  $J = QR$  (see Bates and Watts, 1988). To prevent negative amplitudes, confidence intervals are truncated below zero.

It is useful to verify the coverage of ENOF's approximate 95% confidence intervals, specifically that they are not likely to underestimate the uncertainty. A measure of validity is the fraction of the synthetic tests, described in D.1, for which the true orbital amplitude falls within the range of the estimate's confidence interval. For synthetic time-series featuring orbital variance with SNR = 0 (pure noise), 0.075, 0.25, 0.5, 1, and 2, the 95% confidence interval for the precession amplitude contains the correct amplitude in 94.5%, 97.3%, 98.9%, 99.4%, 99.5%, and 99.6% of tests, indicating that the confidence intervals are conservative.

#### C.2. Sensitivity to choice of window length and shift

It is important to verify that our results are not qualitatively sensitive to the choice of window  $\tau$ , the fitting window length, and  $k$ , the distance between each overlapping windowed fit. Orbital amplitudes are estimated for L2H19 between 3 and 1 Ma when ENOF is run with different combinations of values of  $\tau$  and  $k$ , respectively ranging from 50 to 100 ky and 1 to 6 ky. Using a larger value of  $\tau$  tends to slightly reduce both the precession and obliquity estimates as the algorithm has less flexibility to fit against observations when attempting to fit a single amplitude value over a wider range. Changing  $\tau$  from 50 ky to 100 ky reduces the precession amplitude estimate from 23.5  $\text{meg}^{-1}\text{ky}^{-1}$  to 19.7  $\text{meg}^{-1}\text{ky}^{-1}$  and the obliquity estimate from 37.0  $\text{meg}^{-1}\text{ky}^{-1}$  to 34.0  $\text{meg}^{-1}\text{ky}^{-1}$ . Alternative values of  $\tau$  ranging from 60 to 90 ky give proportional reductions in amplitude estimates relative to  $\tau = 50$  ky. Results are mostly insensitive to changes in  $k$ , with both precession and obliquity estimates changing by 0.1  $\text{meg}^{-1}\text{ky}^{-1}$  or less for values of  $k$  ranging from 1 to 6 ky.

We also repeat the eccentricity-independent test for precession, described in section 5.1, with different combinations of values of  $\tau$  and  $k$ . Wider windows produce a slightly higher correlation with eccentricity because they produce smoother variations. Using  $\tau = 50, 60, 70, 80, 90,$  and  $100$  ky results in correlations of  $A_p$  with eccentricity of 0.46, 0.47, 0.49, 0.50, 0.54, and 0.55. Results are mostly insensitive to the choice of  $k$ , and repeating the tests with values of  $k$  ranging from 1 to 6 ky for each value of  $\tau$  yields a change of 0.01 or less in the correlation of  $A_p$  with eccentricity. We repeated the  $10^4$  phase-randomized trials described in section 5.1 for  $\tau = 100$  ky, which give a 99% significance level

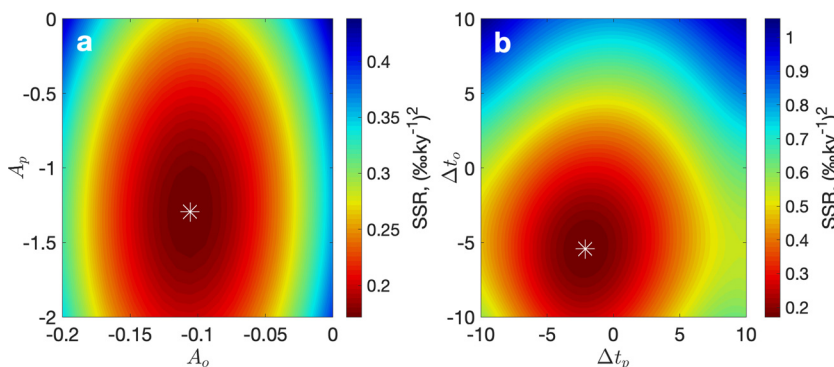


**Fig. C.1.** Comparison of nonlinear least-squares estimates to an exhaustive parameter search. **(a)** Estimates for  $A_p$  and  $A_o$ , where  $\Delta t_p$  and  $\Delta t_o$  are specified as the values estimated by nonlinear least-squares. The white star represents the nonlinear least-squares estimate of the best-fitting combination of parameters, and the contours represent the sum of squared residuals computed by the brute force search. The fit is estimated over a 50 ky period starting at 1.8 Ma in L2H19's smoothed rate-of-change. **(b)** Same as (a), but for estimates of  $\Delta t_o$  and  $\Delta t_p$ , where  $A_p$  and  $A_o$  are specified as the values estimated by nonlinear least-squares.

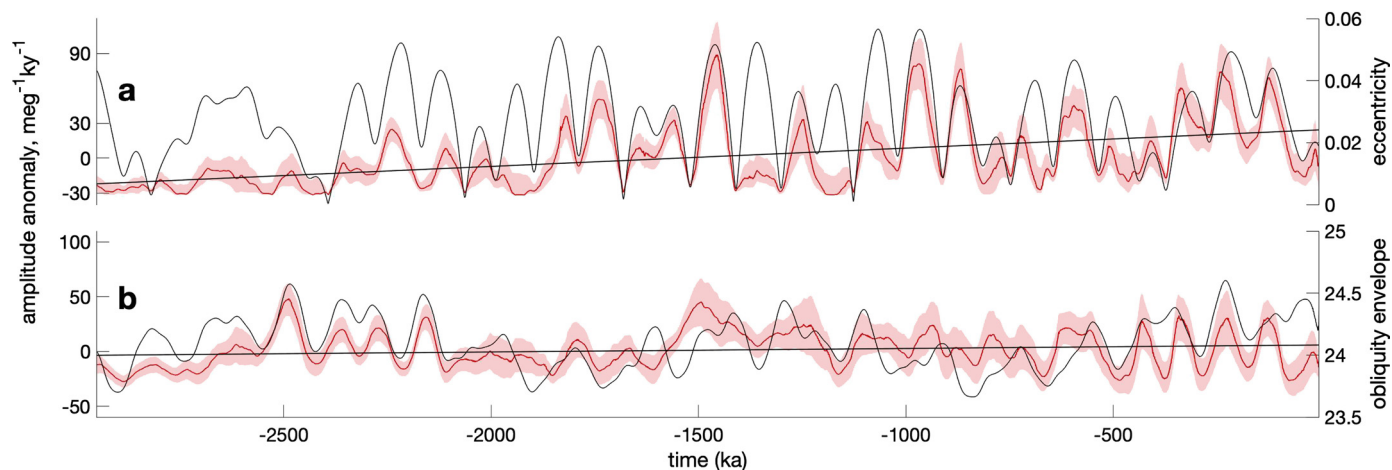


**Fig. C.2.** Trends in orbital forcing in  $d\delta^{18}O/dt$  owing to precession and obliquity over the Pleistocene and late Pliocene using data from L2H19. **(a)** Envelope of the precession contribution from 3 to 0 Ma (red line) and orbital eccentricity (black line). **(b)** same as (a), but for obliquity, and where the black line represents the envelope of obliquity. Envelopes are calculated as the magnitude of the Hilbert transform of the ENOF-estimated precession and obliquity contributions and for the calculated values of obliquity. Shaded areas represent the 95% confidence intervals, and black trend-lines indicate a linear least-squares fit.

of 0.51, compared to a correlation of 0.55 in L2H19, indicating that the significance of the eccentricity-independent test for precession is likely not sensitive to reasonable choices of  $\tau$  or  $k$ .

#### Appendix D. Sensitivity tests for ENOF and spectral analysis

To quantify the sensitivity of orbital amplitude estimates from both ENOF and spectral analysis to (i) the presence of background noise, (ii) the presence of age error, and (iii) differences in sampling resolution, we apply both methods to a common set of synthetic time-series with properties expected to be similar to Pleistocene  $\delta^{18}O$  records.

##### D.1. Sensitivity to noise

Noise introduces bias in both spectral and ENOF estimates. To quantify this bias, we study estimates from both methods when applied to synthetic data. Two competing scenarios are considered in which estimates for a pure noise signal are compared with estimates for synthetic time-series featuring orbital forcing. We adopt a null hypothesis,  $H_0$ , that orbital variability is absent, and estimate  $H_0$ 's distribution with a Monte Carlo approach, applying both methods to  $2.5 \times 10^4$  realizations of noise. Red noise is initially formed following a power law of 2 with a decorrelation frequency of  $1/150 \text{ ky}^{-1}$ , then differenced to produce a mostly white con-

tinuum consistent with observations, as evident in Fig. 1. To form probability distributions associated with the alternate hypothesis that orbital variability is present, we evaluate  $2.5 \times 10^4$  synthetic time-series spanning 2 to 1 Ma featuring climatic precession and obliquity in an average amplitude ratio of 0.55, which is close to the estimated precession-to-obliquity amplitude ratio in orbitally-tuned records between 2 and 1 Ma. Noise with the same properties as in  $H_0$  is then added to the synthetic signal. Six cases, denoted  $H_1$  to  $H_6$ , or  $H_{1-6}$ , are considered, for signal-to-noise ratios of 0.075, 0.25, 0.5, 1, 2, and with no noise. Signal-to-noise ratio is defined here as the variance ratio of the orbital and noise components. The variance of the realized time series, comprising both signal and noise, is fixed such that each distribution features different orbital amplitudes which approach zero as the signal-to-noise ratio approaches zero.

In the absence of noise,  $H_6$ , all estimates in both methods give the true amplitude. In  $H_{1-5}$  the median ENOF estimate exceeds the true precession amplitude by 70%, 28%, 15%, 7%, and 3%, and obliquity by 29%, 10%, 5%, 3%, and 1% (Fig. D.1a,b). Spectral estimates give similar biases if the noise floor is not accounted for, with the median estimate exceeding the true precession amplitude by 82%, 29%, 15%, 8%, and 4% and obliquity by 29%, 9%, 5%, 2%, and 1% (Fig. D.2a,b). These biases are corrected before evaluating  $H_{1-6}$  against  $H_0$ .

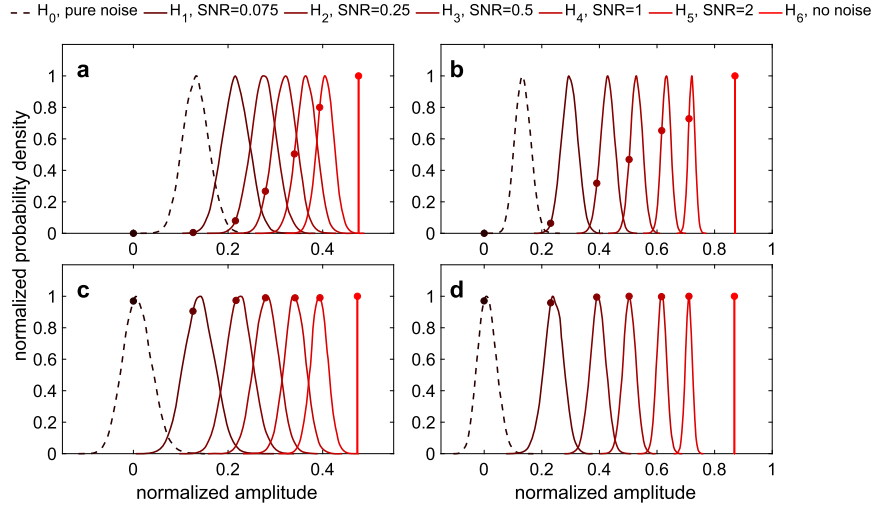


**Fig. D.1.** ENOF estimates for obliquity and precession amplitudes in tests on synthetic time-series with different signal-to-noise ratios. **(a)** Estimates for precession, taken as the square root of the variance of the first term in equation (1), before correcting for noise-induced bias, where each distribution represents  $2.5 \times 10^4$  realizations. **(b)** Same as (a), but for the obliquity estimates, taken as the square root of the variance of the second term in equation (1). **(c)** Same as (a), but after applying the bias correction. **(d)** Same as (b), but after applying the bias correction. Markers indicate the true values as specified in synthetic time-series.

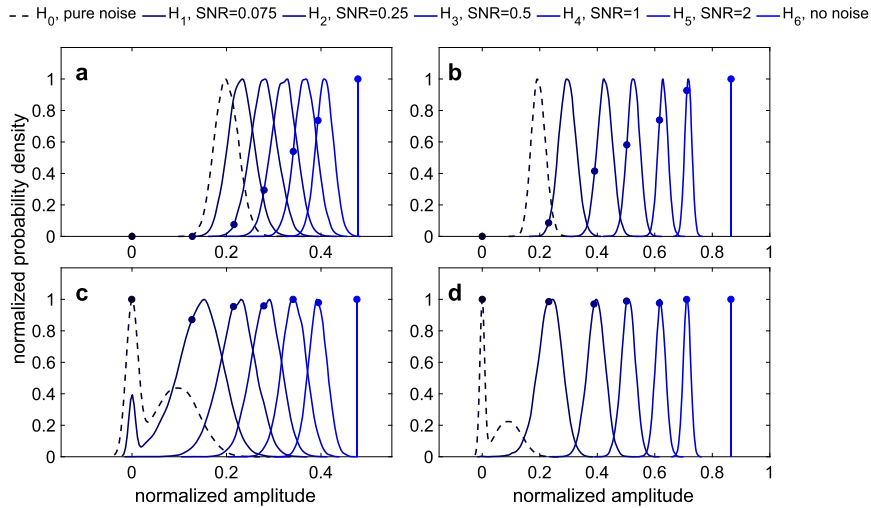


**Fig. D.2.** Spectral estimates of obliquity and precession amplitudes in synthetic tests on time-series with different signal-to-noise ratios. **(a)** Estimates for precession, as described in section 3.1, before correcting for noise-induced bias, where each distribution represents  $2.5 \times 10^4$  realizations. **(b)** Same as (a), but for the obliquity estimates. **(c)** Same as (a), but after applying the bias correction. **(d)** Same as (b), but after applying the bias correction. Markers indicate the true values as specified in synthetic time-series.

The bias associated with ENOF is a function of the amplitude of noise relative to the orbital signal. Determining the correction requires an estimate of the noise fraction of the total amplitude, which is estimated by fitting the background continuum of the power spectrum as done for spectral estimates, then computing the area below the noise level as a fraction of the total area under the power spectrum and taking the square root of this value. A correction amplitude is determined by linearly interpolating the noise fraction with the mean bias from synthetic tests.

In spectral analysis, estimates are bias-corrected by subtracting the noise floor as described in Appendix B. If the variance estimate is negative, an amplitude of zero is assigned to avoid obtaining a complex amplitude estimate when taking the square root of the variance. This, and the distortion introduced by taking the square root of values close to zero, account for the shape of  $H_0$  and the upticks at zero in  $H_0$  and  $H_1$  in Figs. D.2c and D.2d. This distortion does not occur in ENOF estimates because the bias correction is applied after variance is converted to amplitude.

## D.2. Sensitivity to age error

The introduction of age model error, which disperses orbital energy to nearby frequencies, is expected to cause underestimation bias in both methods. ENOF allows for variable time offsets from orbital variations but typically cannot fit age error that exceeds the bounds on  $\Delta t_o$  and  $\Delta t_p$ , though it may recover some amplitude if the age model is incorrect by close to a full orbital cycle. The default bounds of  $\pm 10$  ky allow ENOF to fit almost any precession phase but only covers half of an obliquity cycle.

$10^4$  synthetic time-series are generated with age error,  $\Delta t$ , introduced. Background noise is added with the same properties as described in section D.1 and scaled so that time-series have a signal-to-noise ratio of 0.5. Variability in the sedimentation rate,  $s(t)$ , is first modeled as a random walk, i.e.,  $s_{n+1} = s_n + \eta_n$  where  $\eta_n$  is drawn from a Gaussian distribution (Huybers and Wunsch, 2004), then integrated to give variations in depth with age. Synthetic time-series span 2 to 1 Ma and, following Huybers and

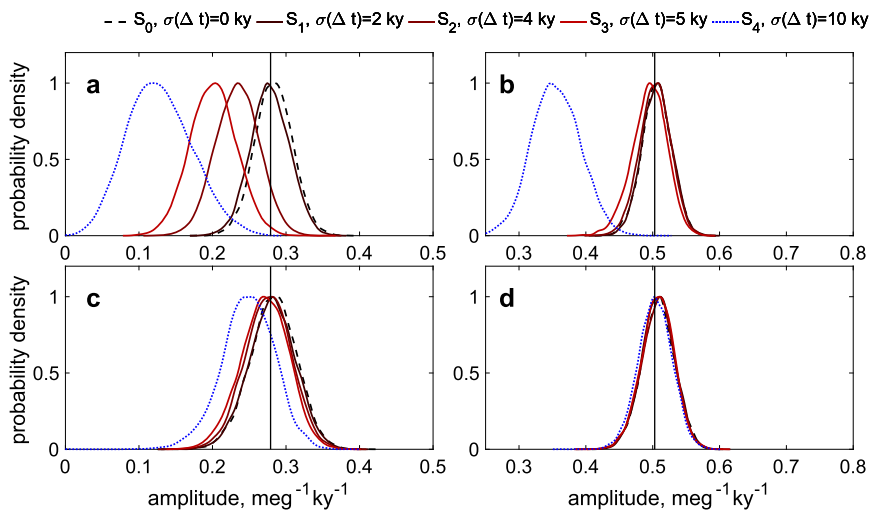


**Fig. D.3.** ENOF and spectral estimates of orbital amplitudes in synthetic time-series disrupted with age error. **a** ENOF precession amplitude estimate with age-error standard deviation ranging from 0 ky (dashed black line), to 10 ky (dotted blue line). Each distribution represents  $10^4$  realizations, and the vertical black line represents the true amplitude. **b** Same as (a), but for obliquity. **c** Same as (a), but where amplitudes are estimated using spectral analysis. **d** Same as (c), but for obliquity.

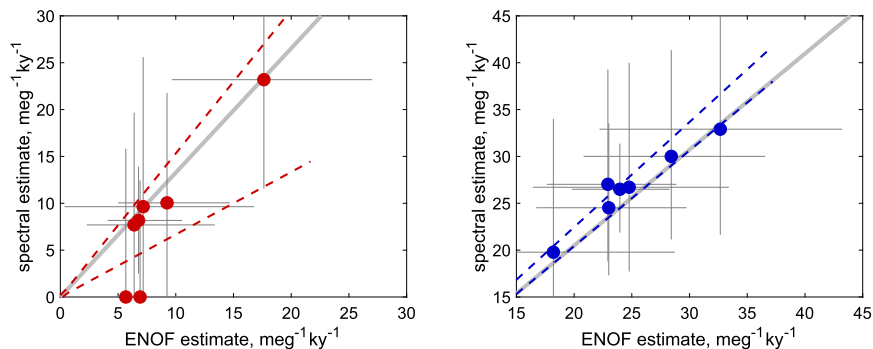


**Fig. D.4.** Expected and observed relationship between ENOF and spectral estimates of orbital amplitudes in the presence of age model error. **(a)** Regression of spectral estimates of precession amplitude against ENOF estimates in  $10^4$  tests on synthetic time-series with  $\text{SNR} = 0.5$  and with age error having a standard deviation of 5 ky (thick gray line). For comparison, also shown are the ENOF and spectral estimates of precession amplitude in  $\delta^{18}\text{O}$  records listed in Table 1 on the depth-derived timescale between 2 and 1 Ma (markers) and their 95% confidence intervals (thin gray bars), as well as the 95% confidence interval for a linear least-squares fit through the markers (dashed lines). Regressions shown here are forced to have zero intercepts. **(b)** same as (a), but for obliquity.

Wunsch (2004), age error is modeled as following a ‘Brownian bridge’, tapering to zero at each endpoint to simulate the increasing amplitude of age error with time away from age-control points. Five cases,  $S_{0-4}$ , are considered.  $S_0$ , having no age error, is identical to  $H_3$  in D.1. In  $S_{1-4}$ ,  $\eta_n$  is scaled such that age model error has a standard deviation of 0, 2, 4, 5, and 10 ky.

There is little to no attenuation in obliquity amplitude estimates for either ENOF or spectral analysis in  $S_{1-3}$ . The average ENOF obliquity amplitude estimates for  $S_{1-3}$  are within 1%, 1%, and 2.2% of that for  $S_0$ . For spectral analysis, the average obliquity attenuation relative to  $S_0$  is less than 1% for  $S_{1-3}$ . The ENOF obliquity estimate is dramatically reduced in  $S_4$ , however, because a standard deviation of 10 ky implies age variations of  $\sim \pm 20$  ky, double the range over which  $\Delta t_o$  and  $\Delta t_p$  are allowed to vary.

ENOF estimates of precession amplitude are generally more sensitive to age error than spectral estimates. Mean amplitude estimates for  $S_{1-3}$  are 1%, 15%, and 25% less than for spectral estimates. A regression of spectral estimates of precession amplitude against ENOF estimates in depth-derived records produces a slope of  $1.07 \pm 0.35$ , and is consistent with the relationship predicted by  $S_3$ , which gives a slope of 1.33 (Fig. D.4). Note that the age error in  $S_3$  is lower than was independently estimated for the depth-derived age model (Huybers, 2007), but that such smaller age errors are also implied by the difference between this age

model and orbitally-tuned records as well as the amplitude of the obliquity signal in depth-derived records.

Estimates of orbital amplitudes are not bias-corrected toward higher values to account for age model error, but are bias corrected toward lower values to account for the presence of noise. The overall result is, therefore, a conservative estimate of orbital amplitude, particularly for precession on account of its being more sensitive to age errors. Although in principle it would be possible to correct estimates for age error, such a correction would inevitably be quite uncertain, and we prefer to make a more conservative test of whether orbital variability is present.

### D.3. Sensitivity to sampling interval

To test the sensitivity of orbital amplitude estimates from both methods to sampling resolution, L2H19 is resampled between 2 and 1 Ma in the depth domain at resolutions ranging from 0.25 ky to 10 ky, then placed on U1308’s tuned age model. Sampling resolution in time is determined using Site U1308’s average sedimentation rate of  $8 \text{ cm ky}^{-1}$  (Hodell and Channell, 2016). ENOF and spectral analysis are repeated for each resampled version of the time series. A clear attenuation of the estimated precession amplitude is observed as the sampling interval increases (Fig. D.5). Precession amplitude estimates are more sensitive to coarsening

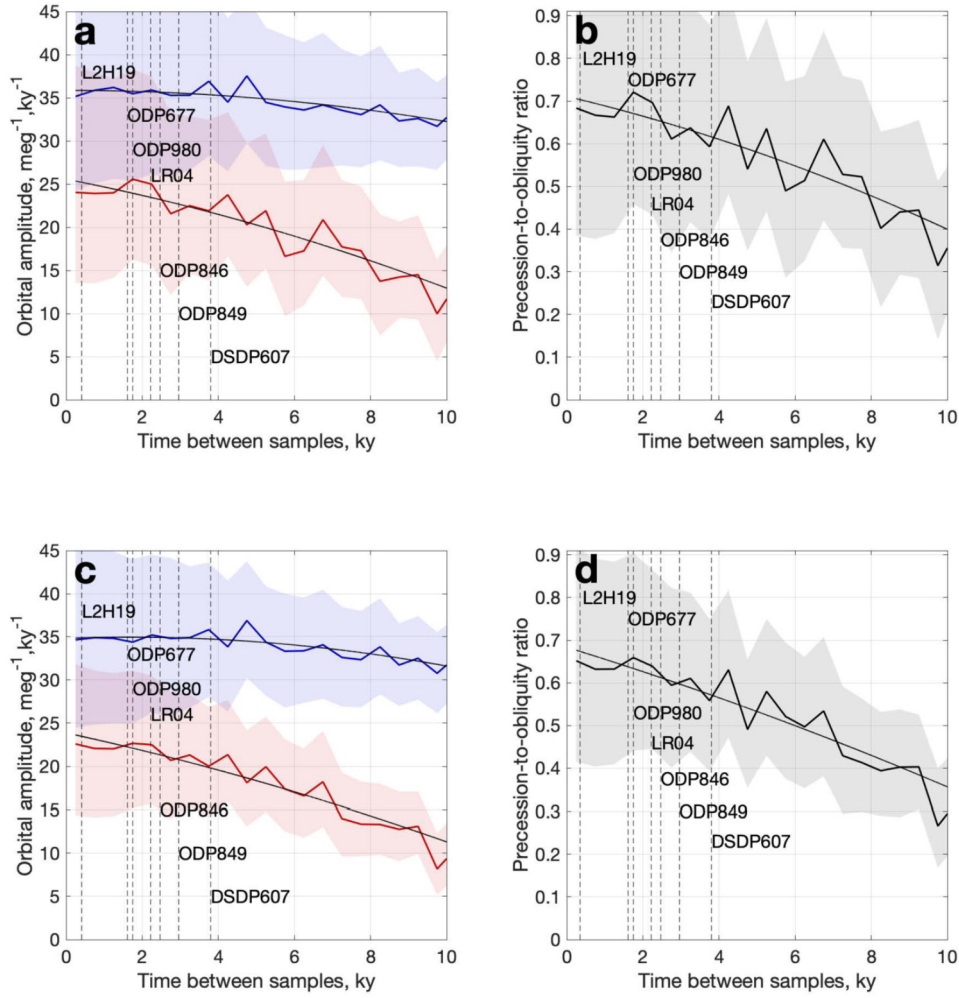


**Fig. D.5.** Effect of coarse sampling on the estimation of orbital amplitudes in benthic  $\delta^{18}\text{O}$  records. **(a)** Spectral estimates of precession (red) and obliquity (blue) amplitudes and their 95% confidence intervals (red and blue shading) in  $d\delta^{18}\text{O}/dt$  between 2 and 1 Ma, using L2H19 on the orbitally-tuned timescale, when L2H19 is resampled in the depth domain at different resolutions. Also indicated are the mean sampling resolution of the records listed in Table 1 over 2-1 Ma (vertical dashed lines). **(b)** The precession-to-obliquity amplitude ratio (black) and its 95% confidence interval (gray shading). **(c)** Same as (a), but using ENOF amplitude estimates. **(d)** Same as (b), but using ENOF amplitude estimates.

of sampling resolution than obliquity on account of its shorter period and its being more heavily amplitude- and frequency-modulated. Thus, coarsening leads to a deterioration of the estimated precession-to-obliquity amplitude ratio (Fig. D.5b,d). Both methods are similarly sensitive to this problem, with ENOF and spectral analysis respectively giving reductions of 15% and 14% in the ratio when resampling L2H19 at the resolution of DSDP 607.

**Appendix E. Ice sheet and energy balance model**

**Table E.3**  
Energy balance constants and parameters for the model described in section 6.

Symbol	Value	Unit	Parameter
$\rho_i$	900	$\text{kg m}^{-3}$	Density of ice
$\rho_w$	1000	$\text{kg m}^{-3}$	Density of water
$\rho_m$	3300	$\text{kg m}^{-3}$	Density of mantle
$\rho_a$	1.5	$\text{kg m}^{-3}$	Density of air
$k_i$	4	$\text{J m}^{-1} \text{K s}$	Thermal conductivity of ice
$k$	0.03	$\text{m}^2/\text{kg}^{-1}$	Mass absorption coefficient, water
$g$	9.8	$\text{m s}^{-2}$	Gravitational acceleration
$\sigma$	$5.67 \times 10^{-8}$	$\text{W m}^{-2} \text{K}^{-4}$	Stefan Boltzmann constant

**Table E.3** (continued)

Symbol	Value	Unit	Parameter
$C_d$	0.011		Drag coefficient
$L_v$	$2.5 \times 10^6$	$\text{J kg}^{-1}$	Latent heat of vaporization
$L_m$	$3.34 \times 10^5$	$\text{J kg}^{-1}$	Latent heat of melting
$L_s$	$2.84 \times 10^6$	$\text{J kg}^{-1}$	Latent heat of sublimation
$a$	$6.37 \times 10^6$	m	Radius of Earth
$K$	273.15	K	Melting temperature of water
$C_p$	2100	$\text{J kg}^{-1} \text{K}^{-1}$	Specific heat capacity, water
$C_{air}$	1.5	$\text{J kg}^{-1} \text{K}^{-1}$	Specific heat capacity, air
$C_{ss}$	$10 \rho_i C_p$	$\text{J m}^{-2} \text{K}^{-1}$	Heat capacity of subsurface layer
$C_s$	$5 \rho_i C_p$	$\text{J m}^{-2} \text{K}^{-1}$	Heat capacity of surface
$C_a$	$5000 \rho_a C_{air}$	$\text{J m}^{-2} \text{K}^{-1}$	Heat capacity of atmosphere
$K_s$	5	J/K	Sensible heat flux coefficient
$H_m$	5200	m	Starting thickness of lower atmospheric layer
$H_{tm}$	2000	m	Thickness of upper atmospheric layer
$\alpha_l$	0.3	-	Land albedo
$\alpha_i$	0.8	-	Ice albedo
$A$	0.2	-	Atmosphere absorption
$R$	0.3	-	Atmosphere reflection
$T$	0.5	-	Atmosphere transmission
$\epsilon_a$	0.85	-	Longwave emissivity
$P$	1	m/a	Precipitation rate
$\Gamma_m$	6.35	K/km	Moist adiabatic lapse rate

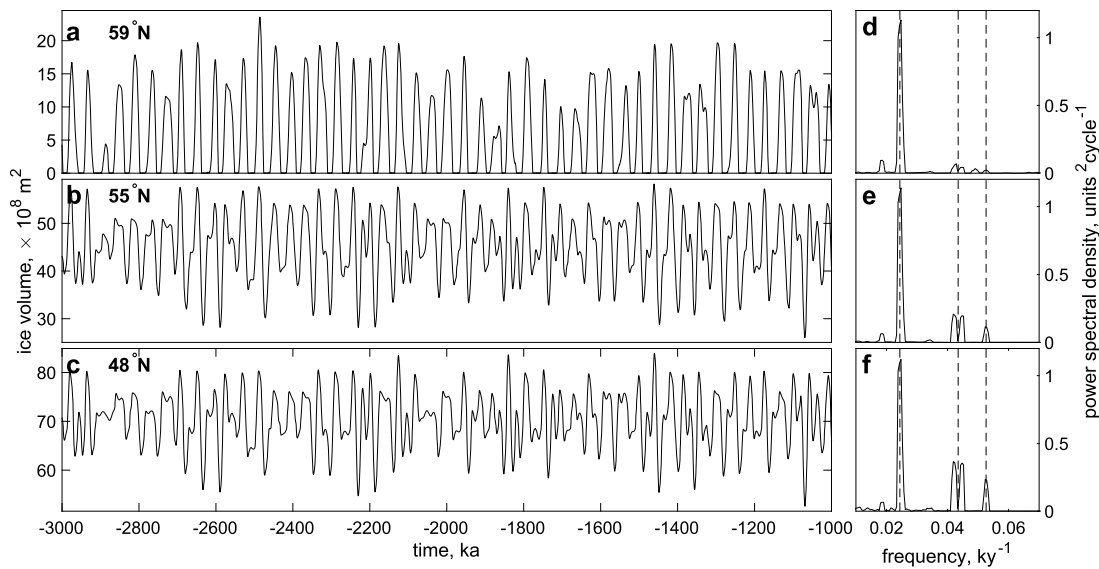


**Fig. E.1.** Model ice volume between 3 and 1 Ma under varying background conditions. (a) Simulated ice volume when a constant emission level of 7.20 km is used, with other parameters as listed in Table E.4. Bold numbers represent the latitude of the southernmost extent of the ice sheet terminus. (b–c) Same as (a), but for emission levels of 6.81 km and 6.50 km. (d–f) Power spectral density for the simulated ice volume curves in panels (a)–(c), normalized by the power at  $1/41 \text{ ky}^{-1}$ , with dashed lines indicating the  $1/41$ ,  $1/23$ , and  $1/19 \text{ ky}^{-1}$  frequencies.

**Table E.4**

Ice sheet and sediment layer parameters for the model described in section 6.

Symbol	Value	Unit	Parameter
$n$	3	-	Glen's law exponent
$m$	1.25	-	Stress-strain law exponent
$A_{ice}$	$7.71 \times 10^{-29}$	$\text{Pa}^{-3} \text{ s}^{-1}$	Ice deformability
$T_b$	5000	yr	Bed depression time
$H_{eq}$	0		Equilibrium surface height
$\rho_s$	2390	$\text{kg m}^{-3}$	Bulk sediment density
$\rho_b$	3370	$\text{kg m}^{-3}$	Bedrock density
$u_o$	$3 \times 10^9$	$\text{Pa} \cdot \text{s}$	Reference sediment viscosity
$h_s$	10	m	Thickness of sediment layer
$D_o$	$2.5 \times 10^{-14}$	$\text{s}^{-1}$	Reference deformation rate
$\phi_{sed}$	22	degrees	Angle of internal friction

### E.1. Sensitivity tests

Ten model simulations spanning 3 to 1 Ma with no background trend in the climate, but different mean climate states, were conducted to test the effect of the background state on the partitioning of orbital energy in simulated ice volume. Supplemental files include all ten runs, with atmospheric radiation emission levels ranging from 6.5 km to 7.2 km. Three runs are displayed in Fig. E.1, and demonstrate a stronger expression of precession when the mean temperature is cooler and the ice sheet terminus lies further south.

Note that other mechanisms not accounted for in the EBM may also influence an ice sheet's response to orbital forcing. For example, a more robust treatment of the temperature dependence of precipitation, which the EBM treats as constant, may influence the net mass balance. Some subglacial mechanisms, such as basal melting, are also neglected, as is the possible role of a partial marine margin and associated ice mass loss by calving.

### References

Adhémar, J., 1842. Révolutions de la mer. Carilian-Goeury et V. Dalmont.  
 Alley, R.B., 1991. Deforming-bed origin for southern Laurentide till sheets? *J. Glaciol.* 37 (125), 67–76.  
 Ashkenazy, Y., Tziperman, E., 2004. Are the 41 kyr glacial oscillations a linear response to Milankovitch forcing? *Quat. Sci. Rev.* 23 (18–19), 1879–1890.  
 Bates, D., Watts, D., 1988. *Nonlinear Regression Analysis and Its Applications*. Wiley.

Berger, A., Li, X., Loutre, M.-F., 1999. Modelling northern hemisphere ice volume over the last 3 Ma. *Quat. Sci. Rev.* 18 (1), 1–11.  
 Berger, A., Loutre, M.-F., 1991. Insolation values for the climate of the last 10 million years. *Quat. Sci. Rev.* 10 (4), 297–317.  
 Bintanja, R., van de Wal, R., 2008. North American ice-sheet dynamics and the onset of 100,000-year glacial cycles. *Nature* 454 (7206), 869.  
 Bintanja, R., van de Wal, R., Oerlemans, J., 2005. Modelled atmospheric temperatures and global sea levels over the past million years. *Nature* 437 (7055), 125.  
 Bolton, C., Wilson, P., Bailey, I., Friedrich, O., Beer, C., Becker, J., Baranwal, S., Schiebel, R., 2010. Millennial-scale climate variability in the subpolar North Atlantic Ocean during the late Pliocene. *Paleoceanography* 25 (4).  
 Bracewell, R.N., 1986. *The Fourier Transform and Its Applications*, vol. 31999. McGraw-Hill, New York.  
 Broecker, W., 1982. Ocean chemistry during glacial time. *Geochim. Cosmochim. Acta* 46 (10), 1689–1705.  
 Broecker, W.S., Thurber, D.L., Goddard, J., Ku, T.-L., Matthews, R., Mesolella, K.J., 1968. Milankovitch hypothesis supported by precise dating of coral reefs and deep-sea sediments. *Science* 159 (3812), 297–300.  
 Burns, J.A., 1976. Elementary derivation of the perturbation equations of celestial mechanics. *Am. J. Phys.* 44 (10), 944–949.  
 Caballero-Gill, R., Herbert, T.D., Dowsett, H., 2019. 100-kyr paced climate change in the Pliocene warm period, southwest Pacific. *Paleoceanogr. Paleoclimatol.* 34 (4), 524–545.  
 Channell, J., Hodell, D., Curtis, J., 2016. Relative paleointensity (RPI) and oxygen isotope stratigraphy at IODP site U1308: North Atlantic RPI stack for 1.2–2.2 Ma (NARPI-2200) and age of the Olduvai Subchron. *Quat. Sci. Rev.* 131, 1–19.  
 Channell, J., Hodell, D., Xuan, C., Mazaud, A., Stoner, J., 2008. Age calibrated relative paleointensity for the last 1.5 myr at IODP site U1308 (North Atlantic). *Earth Planet. Sci. Lett.* 274 (1–2), 59–71.  
 Clark, P., Pollard, D., 1998. Origin of the middle Pleistocene transition by ice sheet erosion of regolith. *Paleoceanogr. Paleoclimatol.* 13 (1), 1–9.  
 Croll, J., 1864. On the physical cause of the change of climate during geological epochs. *Philos. Mag.* 28 (187), 121–137.  
 Duplessy, J.-C., Moyes, J., Pujol, C., 1980. Deep water formation in the North Atlantic Ocean during the last ice age. *Nature* 286 (5772), 479.  
 Elderfield, H., Ferretti, P., Greaves, M., Crowhurst, S., McCave, I., Hodell, D., Piotrowski, A., 2012. Evolution of ocean temperature and ice volume through the mid-Pleistocene climate transition. *Science* 337 (6095), 704–709.  
 Flower, B.P., Oppo, D.W., McManus, J.F., Venz, K., Hodell, D., Cullen, J.L., 2000. North Atlantic intermediate to deep water circulation and chemical stratification during the past 1 Myr. *Paleoceanography* 15 (4), 388–403.  
 Gildor, H., Tziperman, E., 2000. Sea ice as the glacial cycles' climate switch: role of seasonal and orbital forcing. *Paleoceanogr. Paleoclimatol.* 15 (6), 605–615.  
 Hays, J., Imbrie, J., Shackleton, N., et al., 1976. Variations in the Earth's orbit: pacemaker of the ice ages. *Science* 194 (4270), 1121–1132.  
 Hodell, D., Channell, J., 2016. Mode transitions in northern hemisphere glaciation: co-evolution of millennial and orbital variability in quaternary climate. *Clim. Past* 12 (9), 1805–1828.

- Hodell, D.A., Channell, J.E.T., Curtis, J.H., Romero, O.E., Röhl, U., 2008. Onset of "Hudson Strait" Heinrich events in the eastern North Atlantic at the end of the middle Pleistocene transition (~640 ka)? *Paleoceanography* 23 (4).
- Huybers, P., 2006. Early Pleistocene glacial cycles and the integrated summer insolation forcing. *Science* 313 (5786), 508–511.
- Huybers, P., 2007. Glacial variability over the last two million years: an extended depth-derived age model, continuous obliquity pacing, and the Pleistocene progression. *Quat. Sci. Rev.* 26 (1–2), 37–55.
- Huybers, P., Aharanson, O., 2010. Orbital tuning, eccentricity, and the frequency modulation of climatic precession. *Paleoceanography* 25 (4).
- Huybers, P., Tziperman, E., 2008. Integrated summer insolation forcing and 40,000-year glacial cycles: the perspective from an ice-sheet/energy-balance model. *Paleoceanogr. Paleoclimatol.* 23 (1).
- Huybers, P., Wunsch, C., 2003. Rectification and precession signals in the climate system. *Geophys. Res. Lett.* 30 (19).
- Huybers, P., Wunsch, C., 2004. A depth-derived Pleistocene age model: uncertainty estimates, sedimentation variability, and nonlinear climate change. *Paleoceanogr. Paleoclimatol.* 19 (1).
- Imbrie, J., Berger, A., Boyle, E., Clemens, S., Duffy, A., Howard, W., Kukla, G., Kutzbach, J., Martinson, D., McIntyre, A., et al., 1993. On the structure and origin of major glaciation cycles 2. The 100,000-year cycle. *Paleoceanography* 8 (6), 699–735.
- Imbrie, J., Boyle, E., Clemens, S., Duffy, A., Howard, W., Kukla, G., Kutzbach, J., Martinson, D., McIntyre, A., Mix, A., et al., 1992. On the structure and origin of major glaciation cycles 1. Linear responses to Milankovitch forcing. *Paleoceanography* 7 (6), 701–738.
- Imbrie, J., Imbrie, J., 1980. Modeling the climatic response to orbital variations. *Science* 207 (4434), 943–953.
- Kawamura, K., Parrenin, F., Lisiecki, L., Uemura, R., Vimeux, F., Severinghaus, J.P., Hutterli, M.A., Nakazawa, T., Aoki, S., Jouzel, J., et al., 2007. Northern hemisphere forcing of climatic cycles in Antarctica over the past 360,000 years. *Nature* 448 (7156), 912.
- Lawrence, K., Sosdian, S., White, H., Rosenthal, Y., 2010. North Atlantic climate evolution through the Plio-Pleistocene climate transitions. *Earth Planet. Sci. Lett.* 300 (3–4), 329–342.
- Lisiecki, L., 2010. Links between eccentricity forcing and the 100,000-year glacial cycle. *Nat. Geosci.* 3 (5), 349.
- Lisiecki, L., Raymo, M., 2005. A Pliocene-Pleistocene stack of 57 globally distributed benthic  $\delta^{18}O$  records. *Paleoceanography* 20 (1).
- Lisiecki, L.E., Raymo, M.E., 2007. Plio-Pleistocene climate evolution: trends and transitions in glacial cycle dynamics. *Quat. Sci. Rev.* 26 (1–2), 56–69.
- Loutre, M.-F., Paillard, D., Vimeux, F., Cortijo, E., 2004. Does mean annual insolation have the potential to change the climate? *Earth Planet. Sci. Lett.* 221 (1–4), 1–14.
- McIntyre, K., Ravelo, A., Delaney, M., 1999. North Atlantic intermediate waters in the late Pliocene to early Pleistocene. *Paleoceanography* 14 (3), 324–335.
- McManus, J.F., Oppo, D.W., Cullen, J.L., 1999. A 0.5-million-year record of millennial-scale climate variability in the North Atlantic. *Science* 283 (5404), 971–975.
- Milankovitch, M., 1941. *Kanon der Erdbestrahlung und seine Anwendung auf das Eiszeitenproblem*. Royal Serbian Academy Special Publications, vol. 133, pp. 1–633.
- Mix, A.C., Le, J., Shackleton, N., 1995a. Benthic foraminiferal stable isotope stratigraphy of site 846: 0–1.8 Ma. In: *Proceedings of the Ocean Drilling Program. Scientific Results*, vol. 138.
- Mix, A.C., Pisias, N.G., Rugh, W., Wilson, J., Morey, A., Hagelberg, T., 1995b. Benthic Foraminifer Stable Isotope Record from Site 849 (0–5 Ma): Local and Global Climate Changes.
- Murphy, J.J., 1869. On the nature and cause of the glacial climate. *Q. J. Geol. Soc.* 25 (1–2), 350–356.
- Nisancioglu, K., 2004. Modeling the impact of atmospheric moisture transport on global ice volume. PhD thesis. Massachusetts Institute of Technology.
- Oppo, D., McManus, J., Cullen, J., 1998. Abrupt climate events 500,000 to 340,000 years ago: evidence from subpolar North Atlantic sediments. *Science* 279 (5355), 1335–1338.
- Percival, D., Walden, A., 1993. *Spectral Analysis for Physical Applications*. Cambridge University Press.
- Pisias, N., Mix, A., 1988. Aliasing of the geologic record and the search for long-period Milankovitch cycles. *Paleoceanogr. Paleoclimatol.* 3 (5), 613–619.
- Proistosescu, C., Huybers, P., Maloof, A.C., 2012. To tune or not to tune: detecting orbital variability in Oligo-Miocene climate records. *Earth Planet. Sci. Lett.* 325, 100–107.
- Raymo, M., Lisiecki, L., Nisancioglu, K., 2006. Plio-Pleistocene ice volume, Antarctic climate, and the global  $\delta^{18}O$  record. *Science* 313 (5786), 492–495.
- Raymo, M., Nisancioglu, K., 2003. The 41 kyr world: Milankovitch's other unsolved mystery. *Paleoceanography* 18 (1).
- Raymo, M.E., Oppo, D.W., Flower, B.P., Hodell, D.A., McManus, J.F., Venz, K., Kleiven, K., McIntyre, K., 2004. Stability of North Atlantic water masses in face of pronounced climate variability during the Pleistocene. *Paleoceanography* 19 (2).
- Roe, G., 2006. In defense of Milankovitch. *Geophys. Res. Lett.* 33 (24).
- Rubincam, D., 1994. Insolation in terms of Earth's orbital parameters. *Theor. Appl. Climatol.* 48 (4), 195–202.
- Rubincam, D., 2004. Black body temperature, orbital elements, the Milankovitch precession index, and the Seversmith psychroterms. *Theor. Appl. Climatol.* 79 (1–2), 111–131.
- Ruddiman, W., Raymo, M., Martinson, D., Clement, B., Backman, J., 1989. Pleistocene evolution: northern hemisphere ice sheets and North Atlantic Ocean. *Paleoceanogr. Paleoclimatol.* 4 (4), 353–412.
- Ruddiman, W.F., Raymo, M., McIntyre, A., 1986. Matuyama 41,000-year cycles: North Atlantic Ocean and northern hemisphere ice sheets. *Earth Planet. Sci. Lett.* 80 (1–2), 117–129.
- Schreiber, T., Schmitz, A., 2000. Surrogate time series. *Physica D* 142 (3–4), 346–382.
- Shackleton, N., Berger, A., Peltier, W., 1990. An alternative astronomical calibration of the lower Pleistocene timescale based on ODP Site 677. *Earth Environ. Sci. Trans. R. Soc. Edinb.* 81 (4), 251–261.
- Tabor, C., Poulsen, C., Pollard, D., 2015. How obliquity cycles powered early Pleistocene global ice-volume variability. *Geophys. Res. Lett.* 42 (6), 1871–1879.
- Waelbroeck, C., Labeyrie, L., Michel, E., Duplessy, J., McManus, J., Lambeck, K., Balbon, E., Labracherie, M., 2002. Sea-level and deep water temperature changes derived from benthic foraminifera isotopic records. *Quat. Sci. Rev.* 21 (1–3), 295–305.
- Weertman, J., 1964. Rate of growth or shrinkage of nonequilibrium ice sheets. *J. Glaciol.* 5 (38), 145–158.
- Wunsch, C., 2003. The spectral description of climate change including the 100 ky energy. *Clim. Dyn.* 20 (4), 353–363.
- Zeeden, C., Meyers, S.R., Lourens, L.J., Hilgen, F.J., 2015. Testing astronomically tuned age models. *Paleoceanography* 30 (4), 369–383.